This is a preprint, the final version is subject to change, of the American Mineralogist (MSA)
Cite as Authors (Year) Title. American Mineralogist, in press.
DOI: https://doi.org/10.2138/am-2019-6656

Revision 2

Elasticity of single-crystal periclase at high pressure and temperature: the effect of iron on the elasticity and seismic parameters of ferropericlase in the lower mantle

DAWEI FAN[1,2,3,*], SUYU FU[2], JING YANG[2,4], SERGEY N. TKACHEV[5], VITALI B. PRAKAPENKA[5], JUNG-FU LIN[2,*]

[1]Key Laboratory of High Temperature and High Pressure Study of the Earth's Interior, Institute of Geochemistry, Chinese Academy of Sciences, Guiyang, Guizhou 550081, China

[2]Department of Geological Sciences, Jackson School of Geosciences, The University of Texas at Austin, Austin, Texas 78712, U.S.A.

[3]Center for High Pressure Science and Technology Advanced Research (HPSTAR), Shanghai 130012, China

[4]Geophysical Laboratory, Carnegie Institution of Washington, Washington, DC 20015, U.S.A.

[5]Center for Advanced Radiation Sources, University of Chicago, Chicago, Illinois 60437, U.S.A.

[*]Email: fandawei@vip.gyig.ac.cn; afu@jsg.utexas.edu

ABSTRACT:

In this study, we measured the sound velocities of single-crystal periclase by Brillouin light scattering (BLS) combined with *in situ* synchrotron X-ray diffraction (XRD) up to ~30 GPa and 900 K in an externally-heated diamond anvil cell (EHDAC). Our experimental results were used to evaluate the combined effects of pressure and temperature on the elastic moduli of single-crystal periclase using third-order Eulerian finite-strain equations. All of the elastic moduli increased with increasing pressure but decreased with increasing temperature, except the off-diagonal modulus C_{12}, which remained almost constant up to ~30 GPa and 900 K. The derived aggregate adiabatic bulk and shear moduli (K_{S0}, G_0) at ambient conditions were 162.8(±0.2) GPa and 130.3(±0.2) GPa, respectively, consistent with literature results. The pressure

This is a preprint, the final version is subject to change, of the American Mineralogist (MSA)
Cite as Authors (Year) Title. American Mineralogist, in press.
DOI: https://doi.org/10.2138/am-2019-6656

derivatives of the bulk [$(\partial K_S/\partial P)_{300K}$] and shear moduli [$(\partial G/\partial P)_{300K}$] at ambient conditions were 3.94(±0.05) and 2.17(±0.02), respectively, whereas the temperature derivatives of these moduli [$(\partial K_S/\partial T)_P$ and $(\partial G/\partial T)_P$] at ambient conditions were -0.025(±0.001) GPa/K and -0.020(±0.001) GPa/K, respectively. A comparison of our experimental results with the high pressure-temperature (*P-T*) elastic moduli of ferropericlase (Fp) in the literature showed that all the elastic moduli of Fp were linearly correlated with the FeO content up to approximately 20 mol%. These results allowed us to build a comprehensive thermoelastic model for Fp to evaluate the effect of Fe-Mg substitution on the elasticity and seismic parameters of Fp at the relevant *P-T* conditions of the lower mantle. Our modeling results showed that both the increase of the Fe content in Fp and the increasing depth could change the compressional wave anisotropy (AV_P) and shear wave splitting anisotropy (AV_S) of Fp in the upper parts of the lower mantle. Furthermore, using our modeling results here, we also evaluated the contribution of Fp to seismic lateral heterogeneities of thermal or chemical origin in the lower mantle. Both the thermally-induced and Fe-induced heterogeneities ratios ($R_{S/P}=\partial \ln V_S/\partial \ln V_P$) of Fp from 670 to 1250 km along a representative lower mantle geotherm increased by ~2-5% and ~15%, respectively. The thermally-induced $R_{S/P}$ value of Fp20 is ~ 30% higher than Fp10, indicating that the Fe content has a significant effect on the thermally-induced $R_{S/P}$ of Fp. Compared to the seismic observation results ($R_{S/P}$=1.7-2.0) in the upper regions of the lower mantle, the Fe-induced $R_{S/P}$ value of Fp is more compatible than the thermally-induced $R_{S/P}$ value of Fp20 (the expected composition of Fp in the lower mantle) within their uncertainties. Thus, we propose that Fe-induced lateral heterogeneities can significantly contribute to the observed seismic lateral heterogeneities in the Earth's lower mantle (670-1250 km).

Keywords: Elasticity, Periclase, Brillouin Light Scattering, Lower Mantle, Diamond Anvil Cell

This is a preprint, the final version is subject to change, of the American Mineralogist (MSA)
Cite as Authors (Year) Title. American Mineralogist, in press.
DOI: https://doi.org/10.2138/am-2019-6656

INTRODUCTION

Periclase (MgO) is a classic simple oxide that crystallizes in the rock-salt structure with no known experimental phase transition up to 250 GPa at least (e.g., Dorfman et al. 2012; Duffy et al. 1995a; McWilliams et al. 2012). The rock-salt structured MgO also represents one of the most common yet simply structured materials in the deep Earth. The structure can potentially be stable up to approximately 400 GPa based on computational studies and laser shock experiments (e.g., Belonoshko et al. 2010; Coppari et al. 2013; Karki et al. 1997; McWilliams et al. 2012; Oganov et al. 2003). MgO also has very high melting temperatures compared to other mantle minerals (e.g., Ito et al. 2004; Kimura et al. 2017; McWilliams et al. 2012; Tateno et al. 2014; Zerr and Boehler 1994). The wide *P-T* stability of MgO covers relevant high *P-T* conditions of the deep Earth (Duffy and Ahrens 1995) and possibly terrestrial planets or exoplanets (Bolis et al. 2016; Coppari et al. 2013; Duffy et al. 2015). Therefore, precise knowledge of the elastic properties of MgO under high *P-T* conditions is crucial for constructing a reliable mineralogical model of the Earth's lower mantle. There have been an increasing number of studies on the elastic behavior of MgO covering a range of high-pressure or temperature conditions using different techniques, including static XRD (e.g., Dewaele et al. 2000; Fei 1999; Jacobsen et al. 2008; Speziale et al. 2001; Utsumi et al. 1998), BLS (e.g., Murakami et al. 2009, 2012; Sinogeikin and Bass 2000; Zha et al. 2000), ultrasonic interferometry (e.g., Chen et al. 1998; Li et al. 2006; Reichmann et al. 1998; Yoneda 1990), shockwave compressions (e.g., Coppari et al. 2013; Duffy and Ahrens 1995), as well as theoretical studies (e.g., Dorogokupets 2010; Isaak et al. 1990; Karki et al. 1999; Matsui et al. 2000; Wu et al. 2008). To date, however, the elasticity of single-crystal MgO at simultaneous high *P-T* conditions is limited to 8 GPa and 1600 K (Chen et al. 1998), much lower than the *P-T* conditions expected in the lower mantle, which extends at depths corresponding to pressures above 23 GPa.

This is a preprint, the final version is subject to change, of the American Mineralogist (MSA)
Cite as Authors (Year) Title. American Mineralogist, in press.
DOI: https://doi.org/10.2138/am-2019-6656

MgO forms a solid solution with FeO, and in a MgO-rich composition, it is known as ferropericlase (Fp) (Mg,Fe)O while magnesiowustite is named for a FeO-rich composition. In the Earth's lower mantle, Fp is believed to be the second most abundant mineral, co-existing with the most abundant (Al,Fe)-bearing bridgmanite (Bgm) and Ca-perovskite (e.g., Kung et al. 2002; Lin et al. 2005, 2006; Marquardt et al. 2009a, 2009b; Ringwood 1975). Experiments on iron partitioning between Fp and Bgm (K_D= $(Fe/Mg)^{Bgm}$/ $(Fe/Mg)^{Fp}$) at high *P*-*T* conditions suggest that the FeO content in Fp lies in the range of 10-20 mol% for potential compositional models of the lower mantle (e.g., Andrault 2001; Irifune et al., 2010; Mao et al. 1997; Wood 2000). The influences of Fe-Mg substitution on the physical properties of Fp, especially across its electronic spin transition, have recently attracted significant interest to further our understanding of seismic observations and the geodynamical processes of the lower mantle (e.g., Crowhurst et al. 2008; Fei et al. 2007; Lin et al. 2006, 2013; Marquardt et al. 2009; Muir and Brodholt 2015; Wu and Wentzcovitch 2014; Yang et al. 2015). The effect of Fe-Mg substitution on the elastic properties of Fp has been investigated for the whole MgO-FeO system (e.g., Jacobsen et al. 2002; Muir and Brodholt 2015). In particular, previous studies on the effect of FeO in Fp showed that the substitution of FeO strongly increased the density and reduced the velocities of Fp (e.g., Badro et al. 2003; Lin et al. 2013; Muir and Brodholt 2015; Tsuchiya et al. 2006; Yang et al. 2015). However, the fundamental question of how FeO substitution affects the elastic moduli of Fp at high *P*-*T* conditions still needs to be better addressed experimentally.

Recently, there have been a number of studies attempting to characterize the effects of FeO on the full elasticity of Fp at the high *P* or high *P*-*T* conditions of the lower mantle (e.g., Jackson et al. 2006; Jacobsen et al. 2002; Marquardt et al. 2009a; Reichmann et al. 2008; Yang et al. 2015, 2016). Single-crystal XRD and ultrasonic interferometry measurements of the full elastic moduli for a wide range of compositions in the MgO-FeO system at ambient conditions have been documented

(Jacobsen et al. 2002). *In situ* ultrasonic interferometry together with synchrotron XRD measurements on polycrystalline MgO have also been conducted up to 23.6 GPa and 1650 K, and used to establish an independent absolute pressure scale at high *P-T* conditions (Kono et al. 2010; Li et al. 2006; Tange et al. 2009). However, ultrasonic technique measurements are limited in pressure (<30 GPa) and are most readily performed on polycrystalline samples (e.g., Kung et al. 2002; Li et al. 2005, 2006; Li and Zhang 2005), thus, they only provide limited information on the elastic properties of minerals. Nowadays, BLS coupled with diamond anvil cells (DAC) is the most commonly used technique to measure the single-crystal elasticity of mantle minerals (e.g., Duffy et al. 1995b; Fu et al. 2017; Sang and Bass 2014; Sinogeikin and Bass 2002; Wu et al. 2016; Yang et al. 2014). It has tremendous advantages at extremely high *P-T* conditions for optically transparent and translucent samples (e.g., Marquardt et al. 2009a; Yang et al. 2015) and to derive the complete elastic moduli of single-crystal materials (Speziale et al. 2014). BLS has been used to study the single-crystal elasticity of MgO at pressures up to 50 GPa at room temperature (Zha et al. 2000) and temperatures up to 2500 K at room pressure (Sinogeikin et al. 2000, 2004a). Simultaneous high *P-T* single-crystal elasticity studies of the candidate minerals (e.g. olivine, pyroxene, garnet, spinel, ringwoodite, Fp) of the Earth's interior were also reported up to 50 GPa and 1300 K using the BLS technique (e.g., Duan et al. 2018; Lu et al. 2013; Mao et al. 2012, 2015; Yang et al. 2014, 2016; Zhang and Bass 2016). For the single-crystal elasticity of Fp, BLS coupled with an EHDAC was reported up to 50 GPa and 900 K (Yang et al. 2016), while the high-pressure single-crystal elasticity of Fp was reported up to 96 GPa at room temperature (Marquardt et al. 2009a; Yang et al. 2015). However, studying the single-crystal elasticity of Fp with more than 10 mol% FeO (hereafter written as Fp10) is difficult because Fp with a higher amount of FeO is known to be too optically dark to perform the BLS measurement. Using high-pressure inelastic X-ray scattering (IXS) measurements (Fiquet et al. 2004) of the acoustic phonon dispersions of Fp to derive

the full elastic moduli could be a solution to these problems. However, the reported elastic moduli of Fp17 in high-pressure IXS measurements (Antonangeli et al. 2011) have been inconsistent with other experimental results (impulsive stimulated light scattering, and BLS) (e.g., Crowhurst et al. 2008; Marquardt et al. 2009a, 2009b) and theoretical predictions (e.g., Wentzcovitch et al. 2009; Wu et al. 2009). Thus, the reliability of the IXS experimental results has been questioned because the IXS technique is not a direct method to obtain velocities but uses the acoustic phonon dispersions at very high frequencies to extract the velocities (Fiquet et al. 2004), which rises to an inevitable bias in the velocities. Insofar, there is a lack of comprehensive knowledge on the elasticity of MgO and Fp at the relevant high *P*-*T* conditions of the lower mantle.

In this study, we simultaneously measured the acoustic wave velocities and density of single-crystal MgO at high *P*-*T* conditions up to ~30 GPa and 900 K using *in situ* BLS and XRD in an EHDAC. These results were then used to evaluate the high *P*-*T* effects on the sound velocities and elastic moduli of MgO. Using the obtained elastic moduli of MgO at high *P*-*T* conditions as an endmember reference, together with the elastic moduli of Fp from previous BLS studies, we built a comprehensive thermoelastic model of Fp with up to 20 mol% FeO at the high *P*-*T* conditions relevant to lower mantle. We also used these results to evaluate the effects of FeO substitution on the elasticity of Fp, including the acoustic wave velocity anisotropies and seismic parameters. Finally, we used our results to interpret the seismic anisotropy and heterogeneities of the Earth's lower mantle.

EXPERIMENTAL METHODS

A single-crystal MgO platelet of 10 mm × 10 mm square and 0.5 mm thick with (100) crystallographic orientation was purchased from MTI Corporation, which was grown by an arc melting method and natural cooling. The crystal platelet was >99.95% pure with no visible inclusions or microcracking. The X-ray rocking curve of the platelet showed an orientation of <100>±0.2° on the crystal surface. Analysis of the

This is a preprint, the final version is subject to change, of the American Mineralogist (MSA)
Cite as Authors (Year) Title. American Mineralogist, in press.
DOI: https://doi.org/10.2138/am-2019-6656

XRD patterns of the crystal showed a cubic rock-salt structure with a lattice parameter (a) of 4.2163(2) Å and a density (ρ) of 3.58(1) g/cm^3 at ambient conditions.

To prepare our high *P-T* BLS and XRD experiments in an EHDAC, the platelet was polished down on both sides to approximately 20-30 μm thick in the (100) crystallographic orientation using 3M diamond lapping films with an average grainsize of 0.3 microns. The thin polished platelet was then cleaved into several ~ 70 μm × 70 μm square pieces. Round Re disks of 250 μm thick and 3 mm in diameter were pre-indented to 50-60 μm thick using a pair of diamond anvils with 500 μm culets. Subsequently, a cylindrical 250 μm diameter hole was drilled in the pre-indented area and used as the sample chamber. An R-type thermocouple was used for the high-temperature measurements of the sample chamber in the EHDAC (Kantor et al. 2012; Mao et al. 2015; Sinogeikin et al. 2006; Yang et al. 2014, 2016). The thermocouple was attached to one of the diamond surfaces approximately 500 μm away from its culet and cladded with a ceramic adhesive (Resbond 920), which was thermally conductive and electrically insulating. The EHDAC was also equipped with an alumina ceramic holder that was coiled with two Pt wire strings; each was 200 μm diameter and 48 cm in length (Lu et al. 2013; Mao et al. 2015; Yang et al. 2016). The Pt wire heater had a resistance of approximately 1 Ω at ambient conditions. A single-crystal platelet was then placed into the sample chamber, together with gold (Au) powder as the pressure calibrant for the XRD experiments (Fei et al. 2007) as well as a few ruby spheres as pressure indicators for the neon gas-loading (Mao et al. 1986) (Fig. 1a). The neon pressure medium was loaded into the sample chamber using the gas loading system in the Mineral Physics Laboratory of the University of Texas in Austin (Lu et al. 2013; Mao et al. 2015; Yang et al. 2016).

We conducted the high *P-T* BLS combined with XRD measurements at beamline 13-BMD of the GeoSoilEnviroConsortium for the Advanced Radiation Sources (GSECARS) of the Advanced Photon Source (APS), Argonne National Laboratory (ANL). An incident X-ray beam of 0.3344 Å wavelength focused to 7×20 μm^2

diameter (Sinogeikin et al. 2006) was used to confirm the platelet orientation and to determine the unit cell volume of the crystal in the EHDACs. To avoid oxidation and failure of the diamond anvils and Pt wires at high temperature, the EHDAC was mounted inside a water-cooled holder with 150 μm thick silica glass windows, and Ar with 2% H_2 gas mixture continuously flowed through the EHDAC during heating (Sinogeikin et al. 2006). To minimize pressure instability for each given heating run, the sample chamber was heated to a given temperature and then stabilized for at least 30 minutes, and its pressure was continuously monitored using XRD until the pressure was sufficiently stable for the BLS experiments. The pressure was determined from the measured lattice parameters of Au at high *P*-*T* using the third-order Birch-Murnaghan equation of state of Au (Fei et al. 2007), and the temperature of the sample chamber was from the thermocouple measurements. BLS measurements were only conducted when no significant change in pressure was confirmed by the analysis of the XRD patterns of the Au calibrant. To ensure the pressure stability of the experiments a series of XRD patterns of the Au pressure calibrant were collected before and after the BLS measurements of pressure determinations at high *P*-*T*. The pressure uncertainties were determined using multiple measurements from the pressures before and after the BLS measurements for each *P*-*T* point. Temperatures of the sample chamber were actively stabilized within ±1 K using the temperature-power feedback program with a remotely controlled Tektronix Keithley DC power supply during the experiments (Sinogeikin et al. 2006). The uncertainties of the unit-cell parameters of MgO were typically in the order of 0.03% (Table 1), indicating that the MgO sample remained sufficiently high quality for the XRD and BLS experiments at high *P*-*T* conditions. Analysis of the XRD pattern of the sample was used to determine the density of MgO at each *P*-*T* condition before and after the BLS measurements.

The single-crystal XRD patterns (Fig. 1b) were also taken to verify the [100] crystallographic direction of the MgO platelet before carrying out the BLS

This is a preprint, the final version is subject to change, of the American Mineralogist (MSA)
Cite as Authors (Year) Title. American Mineralogist, in press.
DOI: https://doi.org/10.2138/am-2019-6656

measurements. Then, the motorized DAC rotation stage, which was perpendicular to the focused X-ray beam, was rotated by 45° to get the [110] crystallographic direction of the MgO platelet. Analysis of the XRD spots of the MgO crystal showed a high-quality single crystal nature with a typical FWHM (full width at half maximum) of a diffraction peak at ±0.2° (Fig. 1b). High *P-T* BLS spectra of the single-crystal MgO along the [100] and [110] crystallographic directions as well as XRD spectra were collected up to ~30 GPa at selected temperatures of 300 K, 500 K, 700 K, and 900 K (Figs. 2 and 3, and Table 1). The Brillouin system was equipped with a Coherent Verdi V2 solid-state laser with a wavelength of 532 nm, and a laser head power of 0.4 W was used for the BLS measurements. BLS spectra were collected in the symmetric forward scattering geometry with an external scattering angle of 50° using a six-pass Sandercock-type piezoelectrically scanning tandem Fabry-Pérot interferometer (Sandercock 1982). The interferometer was equipped with a Perkin Elmer MP983 photocounting module with a low dark count rate of <2 counts/s at room temperature (Sinogeikin et al. 2006). The laser beam focused on the sample position was approximately 15 μm in diameter. The external scattering angle of the system was calibrated using silicate glass and distilled water standards (Ostwald et al. 1977; Polian et al. 2002). The acoustic V_P and V_S velocities of the sample were derived from the analysis of the measured Brillouin frequency shift as follows:

$$V_{P,S}=(\lambda_0\Delta\nu_B)/2\sin(\theta/2) \quad (1)$$

where $V_{P,S}$ is the acoustic compressional or shear wave velocity, respectively, λ_0 is the incident laser wavelength of 532 nm, $\Delta\nu_B$ is the Brillouin frequency shift, and θ is the external scattering angle of 50°.

RESULTS

Our collected BLS spectra along the [100] and [110] crystallographic directions showed strong V_P and V_S peaks with high signal-to-noise ratios at high *P-T* conditions (Fig. 2). Although two polarized V_S peaks were expected to exist, only one V_S peak

This is a preprint, the final version is subject to change, of the American Mineralogist (MSA)
Cite as Authors (Year) Title. American Mineralogist, in press.
DOI: https://doi.org/10.2138/am-2019-6656

was observed in our study. This is a result of the polarization of the V_S in the (100) crystallographic orientation of the MgO crystal interacting with the incident laser. Brillouin signals of the neon pressure medium were also observed at pressures below ~ 8 GPa, but they were too weak to be visible in the BLS spectra when the pressure was increased above approximately 8 GPa (Fig. 2). Analysis of the V_P and V_S velocities of MgO as a function of pressure at each given temperature showed that the V_P along the [100] and [110] directions as well as V_S along the [110] direction (hereafter written as V_P[100], V_P[110], and V_S[110], accordingly) increased with increasing pressure and decreased with increasing temperature. However, V_S along the [100] (hereafter written as V_S[100]) remained almost unaffected by increasing *P*-*T* up to ~30 GPa and 900 K (Fig. 4). These observations indicate strong *P*-*T* effects on the V_S anisotropy.

The elastic tensors of cubic MgO can be fully described by three independent elastic moduli, C_{11}, C_{12}, and C_{44}. The use of the (100) platelets in this study permits determination of the elastic moduli (C_{11}, C_{12}, C_{44}) using the velocity determined in the [100] and [110] directions (Fig. 5), respectively, together with the measured density (Table 2). The equations used in the analysis were derived from Christoffel's equation (Grimsditch 2001):

$$\rho V^2_P[100]=C_{11} \quad (2)$$

$$\rho V^2_S[100]=C_{44} \quad (3)$$

$$\rho V^2_P[110]=(C_{11}+2C_{44}+C_{12})/2 \quad (4)$$

$$\rho V^2_S[110]=(C_{11}-C_{12})/2 \quad (5)$$

where ρ is the density of MgO; V_P[100] and V_S[100] are the measured compressional- and shear-wave velocities of MgO along the [100] direction, respectively; V_P[110] and V_S[110] are the compressional- and shear-wave velocities along the [110] direction, respectively; and C_{11}, C_{12}, and C_{44} are the compressional, off-diagonal, and shear moduli of MgO, respectively. We used the least squares regression method

This is a preprint, the final version is subject to change, of the American Mineralogist (MSA)
Cite as Authors (Year) Title. American Mineralogist, in press.
DOI: https://doi.org/10.2138/am-2019-6656

utilizing the aforementioned four equations instead of only three equations for the modeling because examination of equations (2-5) showed that the three elastic moduli (C_{11}, C_{12}, and C_{44}) could be determined more accurately. The uncertainties of the elastic moduli (Table 2) were estimated using standard error propagation in these derivations. We should note that these equations were derived from the general Christoffel's equation (Every1980):

$$\left|\Gamma_{ij} - \rho V^2 \delta_{ij}\right| = 0 \quad (6)$$

where ρ is the density from XRD measurements, V is the measured acoustic velocity, δ_{ij} is the Kronecker delta, and Γ_{ij} is the coefficient in the Christoffel matrix. The values of the Christoffel coefficients (Γ_{ij}) depend on the single-crystal constants (C_{ij}) in the reduced Voigt notation, where the propagation direction of the sound velocity is described by the direction cosines of the acoustic wavevector, n_i.

Using the derived elastic moduli of MgO, we calculated the aggregate adiabatic bulk and shear moduli (K_S and G) (Table 1 and Fig. 6 a, b) using the Voigt-Ruess-Hill averages (Hill 1952):

$$K_S = C_{11} - 2C/3 \quad (7)$$

$$G = [(C/5 + 3C_{44}/5) + 5C_{44}C/(4C_{44} + 3C)]/2 \quad (8)$$

$$C = C_{11} - C_{12} \quad (9)$$

The derived K_{S0} and G_0 at ambient conditions were 162.8(±0.2) GPa and 130.3(±0.2) GPa, respectively. The aggregate velocities of MgO (Fig. 6 c, d) were calculated using the equations:

$$V_P = \sqrt{(K_S + 4G/3)/\rho} \quad (10)$$

$$V_S = \sqrt{G/\rho} \quad (11)$$

This is a preprint, the final version is subject to change, of the American Mineralogist (MSA)
Cite as Authors (Year) Title. American Mineralogist, in press.
DOI: https://doi.org/10.2138/am-2019-6656

The pressure and temperature derivatives of the elastic moduli were obtained by fitting the experimental data using the third-order finite strain equations (Tables 3 and 4) (Birch 1978; Duffy and Anderson 1989):

$$C_{ij}(T) = (1+2f)^{7/2}[C_{ij0}(T) + a_1 f] + a_2 P \quad (12)$$

$$C_{ij0}(T) = C_{ij0}(300\text{K}) + (\text{T-300})(\partial C_{ij}/\partial T)_P \quad (13)$$

$$a_1 = 3K_{T0}(T)[(\partial C_{ij}/\partial P)_T - a_2] - 7C_{ij0}(T) \quad (14)$$

$$f = (1/2)[(V_0(\text{T})/V)^{2/3} - 1] \quad (15)$$

$$V_0(\text{T}) = V_0(300\text{K}) exp \int_{300}^{T} \alpha \, dT \quad (16)$$

$$(\partial C_{ij}/\partial P)_T = (\partial C_{ij}/\partial P)_{300K} \, exp \int_{300}^{T} \alpha \, dT \quad (17)$$

where P is the measured pressure; C_{ij0}(300 K) is the elastic modulus at ambient conditions; $C_{ij0}(T)$ is the elastic modulus at temperature T and 1 bar; $C_{ij}(T)$ is elastic modulus at temperature T and high pressures; $(\partial C_{ij}/\partial T)_P$ is the temperature derivative of the elastic modulus at constant P and ambient T; $(\partial C_{ij}/\partial P)_T$ is the pressure derivative of the elastic modulus at constant T and ambient P; $(\partial C_{ij}/\partial P)_{300K}$ is the pressure derivative of the elastic modulus at ambient conditions; a_2 equals 3 for C_{11} and 1 for C_{12} and C_{44}; and f is the finite strain; V is the volume at high P-T determined by single-crystal XRD; V_0(T) is the volume at 1 bar and high temperature T; V_0(300K) is the volume at ambient conditions; and α is the thermal expansion coefficient at ambient conditions. $K_{T0}(T)$ is the isothermal bulk modulus at temperature T and 1 bar, and can be calculated as:

$$K_{T0} = K_{T0}(300\text{ K}) + (\partial K_T/\partial T)_P \, (T\text{-}300) \quad (18)$$

$$K_{T0}(300) = K_{S0}(300\text{K})/(1+\alpha\gamma\times 300) \quad (19)$$

$$(\partial K_T/\partial T)_P \backsimeq (\partial K_S/\partial T)_P /(1+\alpha\gamma T) - K_S(\text{T})/(1+\alpha\gamma T)^2[\alpha\gamma + \gamma T\times(\partial\alpha/\partial T)] \quad (20)$$

where α is the thermal expansion coefficient at ambient conditions, and γ is the Grüneisen parameter at ambient conditions with a literature value of 1.442 (Tange et

This is a preprint, the final version is subject to change, of the American Mineralogist (MSA)
Cite as Authors (Year) Title. American Mineralogist, in press.
DOI: https://doi.org/10.2138/am-2019-6656

al. 2009). The temperature derivative of K_S, $(\partial K_S/\partial T)_P$, and the pressure derivative of K_S, $(\partial K_S/\partial P)_T$, were derived by fitting K_S at high *P-T* using the third-order finite strain equations (Tables 3 and 4):

$$K_S=K_{S0}(1+2f)^{5/2}\{1+[3(\partial K_S/\partial P)_T-5]f\} \quad (21)$$

$$K_{S0}=K_{S0}(300\text{K})+(\partial K_S/\partial T)_P(T-300) \quad (22)$$

$$(\partial K_S/\partial P)_T=(\partial K_S/\partial P)_{300}\ exp\int_{300}^{T}\alpha\, dT \quad (23)$$

where K_{S0}(300 K) is the adiabatic bulk modulus at ambient conditions, $K_{S0}(T)$ is the adiabatic bulk modulus at temperature T and 1 bar, $K_S(T)$ is the adiabatic bulk modulus at temperature T and high pressures, and $(\partial K_S/\partial P)_{300K}$ is the pressure derivative of K_S at ambient conditions. We also constrained the pressure and temperature derivatives of the shear modulus G of MgO using the third-order finite strain equations:

$$G(T)=(1+2f)^{5/2}[G_0(T)+b_1f] \quad (24)$$

$$G_0(T)=G_0(300\text{K})+(\partial G/\partial T)_P\,(T-300) \quad (25)$$

$$b_1=3K_{S0}(T)(\partial G/\partial P)_T-5G_0(T) \quad (26)$$

$$(\partial G/\partial P)_T=(\partial G/\partial P)_{300K}\ exp\int_{300}^{T}\alpha\, dT \quad (27)$$

where G_0(300K) is the shear modulus at ambient conditions; $G_0(T)$ is the shear modulus at temperature T and 1 bar; $G(T)$ is the shear modulus at temperature T and high pressures; $(\partial G/\partial P)_T$ and $(\partial G/\partial T)_P$ are the pressure and temperature derivatives of the shear modulus, respectively, and $(\partial G/\partial P)_{300K}$ is the pressure derivative of the shear modulus at ambient conditions (Tables 3-4).

DISCUSSION

The single-crystal elasticity of MgO at high *P-T*

By combining the BLS and single-crystal XRD measurements, we derived the full single-crystal elasticity of MgO at simultaneously high *P-T* conditions, including all

This is a preprint, the final version is subject to change, of the American Mineralogist (MSA)
Cite as Authors (Year) Title. American Mineralogist, in press.
DOI: https://doi.org/10.2138/am-2019-6656

of the elastic moduli (C_{ij}s, K_S, and G) (Figs. 5 and 6, Tables 1 and 2). All C_{ij}s and K_S exhibit a linear increase with pressure at the given temperatures (Figs. 5 and 6a), whereas G shows a slight pressure-dependent concave curvature (Fig. 6b). Compared with the values from ultrasonic interferometry and BLS experiments, the derived pressure derivatives for the compressional moduli C_{11}, off-diagonal moduli C_{12}, and bulk modulus K_S at ambient conditions in this study are slightly lower than the corresponding values in the literature (Jackson and Niesler 1982; Kono et al. 2010; Li et al. 2006; Sinogeikin and Bass 2000; Yoneda 1990), except the pressure derivative of C_{12} and K_S from previous BLS studies (Sinogeikin and Bass 2000; Zha et al. 2000), which are consistent with the results in this study. This indicates an enhanced temperature effect on these elastic moduli at high pressures. In addition, the pressure derivatives of the shear moduli (C_{44} and G) at ambient conditions are indistinguishable from the values in previous studies within experimental uncertainties (Tables 3 and 4), except a larger pressure derivative of G at ambient conditions was reported by Zha et al. (2000) and a smaller pressure derivative of C_{44} was reported by Sinogeikin and Bass (20000). These discrepancies potentially due to the limited experimental pressure range or the possible distortion or deformation of MgO under high-pressure condition. At high temperature, all the elastic moduli follow similar trends with pressures (Figs. 5 and 6): increasing temperature offsets of C_{ij}s to a lower value at a given pressure, with the exception of those for the off-diagonal modulus C_{12}, which remain almost constant up to ~30 GPa and 900 K (Fig. 5). The temperature derivatives of the elastic moduli derived from our simultaneously high P-T measurements are consistent with literature experimental and theoretical results within their uncertainties (Tables 3 and 4). In particular, our $(\partial G/\partial T)_P$ is -0.020(1) GPa/K, which is in excellent agreement with another result (-0.020(1) GPa/K) from high P-T BLS measurements on polycrystalline MgO at T=2700 K and P up to 68.4 GPa (Murakami et al. 2012). However, our $(\partial K_S/\partial T)_P$ is -0.025(1) (GPa/K), whose absolute value is slightly larger than those of most

377 literature values (Isaak et al. 1989; Karki et al. 1999; Kono et al. 2010; Sinogeikin et
378 al. 2000; Sumino et al. 1983), except the computational value of -0.028 (GPa/K) by
379 Matsui et al. (2000). It is also worth noting that the temperature derivative of our C_{12}
380 is very consistent with an earlier reported value obtained at 1 bar and high
381 temperature (Sinogeikin et al. 2000), but it is substantially lower than previous
382 rectangular parallelepiped resonance (RPR) experimental results (Isaak et al. 1989;
383 Sumino et al. 1983) and a computational result (Karki et al. 1999). These
384 discrepancies may be caused by the potential systematic errors in different
385 experimental or theoretical methods.

386 **Compressional wave velocity and shear wave splitting anisotropy of MgO**

387 The elastic wave anisotropy of minerals expresses the difference in stiffness of a
388 structure in different crystallographic directions, and shear wave anisotropy can be an
389 indicator of the stability of minerals (Sinogeikin and Bass 2000). Knowledge of the
390 velocity anisotropy of minerals at high *P*-*T* conditions may help to explain the seismic
391 anisotropy within the Earth's interior (Long and Becker 2010; Mainprice 2015). To
392 understand the evolution of the velocity anisotropy of MgO at high *P*-*T* conditions,
393 the V_P and V_S velocities at different propagation directions and anisotropy
394 distributions were calculated using our derived C_{ij}s and density at each given *P*-*T*
395 point (Mainprice 1990; Mainprice et al. 2000). The percentage anisotropy for V_P (AV_P)
396 is defined here as:

397 $$AV_P = (V_{P,max}-V_{P,min}) /(V_{P,max}+V_{P,min}) \times 200\ \% \quad (28)$$

398 where $V_{P,max}$ and $V_{P,min}$ represent the maximum and minimum V_P velocities,
399 respectively. The polarization anisotropy factor of V_S (AV_S), also called the shear
400 wave splitting factor, is the anisotropy percentage of the two V_S in a given direction
401 and is defined as:

402 $$AV_S = (V_{S1}-V_{S2}) /V_S \times 100\ \% \quad (29)$$

This is a preprint, the final version is subject to change, of the American Mineralogist (MSA)
Cite as Authors (Year) Title. American Mineralogist, in press.
DOI: https://doi.org/10.2138/am-2019-6656

where V_{S1} and V_{S2} are the two orthogonally polarized V_S velocities in the given propagation direction and V_S represents the aggregate shear wave velocity. A contoured upper hemisphere stereogram of V_P and AV_S for MgO at two representative *P-T* conditions from our experiments is shown in Figure 7. These results show that, even though MgO is highly anisotropic at ambient conditions, with an AV_P of 11.0% and AV_S of 21.5% (Fan et al. 2015; Mainprice 2015), AV_P reduces to 7.1% and AV_S to 14.1% at 7.17 GPa and 500 K in this study (Fig. 7). AV_P and AV_S decrease to 0.5% and 1.2%, respectively, at the maximum *P-T* conditions of 29.63 GPa and 900 K in our experiments, showing that MgO is almost elastically isotropic at such high *P-T* conditions (Fig. 7). These results clearly show that high *P-T* have a significant impact on the elastic wave velocity anisotropy of MgO.

Modeling the elasticity of (Mg,Fe)O ferropericlase at high *P-T* conditions

MgO is an endmember of (Mg,Fe)O ferropericlase, the second most abundant mineral in the lower mantle. Since the (Mg,Fe)O solid solution system crystallizes in the rock-salt structure at relevant lower-mantle *P-T* conditions, it is possible to use our MgO results as an endmember reference for understanding the elasticity of the (Mg,Fe)O system at high *P-T* conditions. In order to model the elasticity of Fp with different FeO contents at high *P-T* conditions, we initially compared our MgO results to literature elasticity values of Fp (Fp1, Fp6, Fp10) derived from Brillouin measurements (Marquardt et al. 2009a; Reichmann et al. 2008; Yang et al. 2016) (Figs. 8 and 9). Considering the limited available single-crystal elastic moduli results of Fp from other methods (Antonangeli et al. 2011; Crowhurst et al. 2008; Jacobsen et al. 2002), and avoiding the potential systematic errors in different experimental methods (for example, incompatible results by IXS methods with other available studies; the possible effect on the pressure derivatives of elastic moduli by ultrasonic methods vs Brillouin scattering), we only used literature Brillouin results in our modeling. We also limited the modeling to Fp with up to 20 mol% FeO because of the limited Fp compositions in the literature (Marquardt et al. 2009a; Reichmann et al.

This is a preprint, the final version is subject to change, of the American Mineralogist (MSA)
Cite as Authors (Year) Title. American Mineralogist, in press.
DOI: https://doi.org/10.2138/am-2019-6656

2008; Yang et al. 2016) and the relevant Fp composition of approximately Fp20 in the Earth's lower mantle (Andrault 2001; Irifune et al. 2010; Mao et al. 1997; Ringwood 1975; Wood 2000).

Our analysis of the single-crystal elastic moduli (C_{ij}) of MgO as a function of the FeO content in mol% at ambient conditions showed that the substitution of FeO in Fp had a positive effect on C_{12} and a negative effect on C_{11} and C_{44}. Within experimental uncertainties, C_{12} linearly increased with FeO content, while C_{11} and C_{44} decreased linearly with increasing FeO content (Fig. 8):

$$C_{11}= 296.8(\pm1.8)-184.5(\pm30.4)X_{Fe} \quad (30)$$

$$C_{12}= 95.6(\pm0.7)+71.3(\pm12.6)X_{Fe} \quad (31)$$

$$C_{44}= 152.7(\pm0.2)-108.4(\pm2.9)X_{Fe} \quad (32)$$

where $X_{Fe}=M_{FeO}/(M_{FeO}+M_{MgO})$, X_{Fe} is the mole fraction, and M_{MgO} and M_{FeO} are the molar content. In addition, Jacobsen et al. (2002) reported the effects of FeO substitution on the C_{ij} values of (Mg,Fe)O using ultrasonic interferometry with high-frequency shear waves at ambient conditions. They fitted their C_{ij} values of the MgO-FeO system using a second-order or a third-order polynomial. A close inspection of the polynomial fits showed that there was a close linear relationship between the C_{ij} and FeO content when the FeO content in Fp is less than 20 mol% (as shown by the dashed lines in Fig. 8). Thus, we used the linear relationship between the C_{ij} and FeO content of Fp at ambient conditions as a fitting parameter in our modeling here.

We also evaluated the high *P-T* relationship between the C_{ij} and FeO content by comparing the pressure and temperature derivatives of the single-crystal elastic moduli (C_{ij}) of MgO [$(\partial C_{ij}/\partial P)_{300K}$ and $(\partial C_{ij}/\partial T)_P$] to the literature results of Fp (Fp6, Fp10) (Marquardt et al. 2009a; Yang et al. 2016). Analysis of these results showed that within experimental uncertainties, $(\partial C_{11}/\partial P)_{300K}$ and $(\partial C_{12}/\partial P)_{300K}$ increased

This is a preprint, the final version is subject to change, of the American Mineralogist (MSA)
Cite as Authors (Year) Title. American Mineralogist, in press.
DOI: https://doi.org/10.2138/am-2019-6656

457 linearly with increasing FeO content, but $(\partial C_{44}/\partial P)_{300K}$ decreased linearly with
458 increasing FeO content (Fig. 9a):

459 $$(\partial C_{11}/\partial P)_{300K} = 8.43(\pm0.13)+2.68(\pm1.89)X_{Fe} \quad (33)$$

460 $$(\partial C_{12}/\partial P)_{300K} = 1.46(\pm0.09)+2.00(\pm1.22)X_{Fe} \quad (34)$$

461 $$(\partial C_{44}/\partial P)_{300K} = 1.25(\pm0.01)-4.31(\pm0.09)X_{Fe} \quad (35)$$

462 Since the experimental temperature derivatives of C_{ij} $[(\partial C_{ij}/\partial T)_P]$ of Fp were only
463 available for Fp6 (Yang et al. 2016), we calculated the $(\partial C_{ij}/\partial T)_P$ of Fp10 using the
464 C_{ij}s at ambient conditions obtained by Marquardt et al. (2009a) and C_{ij}s at high
465 temperatures up to 4000 K obtained by Muir and Brodholt (2015). The results above
466 were then used to estimate the effect of FeO on the $(\partial C_{ij}/\partial T)_P$ of Fp. Within
467 uncertainties, these results showed that $(\partial C_{11}/\partial T)_P$ and $(\partial C_{12}/\partial T)_P$ increased with
468 increasing FeO content, while $(\partial C_{44}/\partial T)_P$ decreased with increasing FeO content.
469 Therefore, we fitted the data with a linear relationship between the $(\partial C_{ij}/\partial T)_P$ and FeO
470 content in Fp (Fig. 9b):

471 $$(\partial C_{11}/\partial T)_P = -0.063(\pm0.003)+0.11(\pm0.03)X_{Fe} \quad (36)$$

472 $$(\partial C_{12}/\partial T)_P = 0.0010(\pm0.0006)+0.08(\pm0.01)X_{Fe} \quad (37)$$

473 $$(\partial C_{44}/\partial T)_P = -0.01(\pm0.001)-0.10(\pm0.02)X_{Fe} \quad (38)$$

474 These derived linear relationships for the elastic moduli and their *P*-*T* derivatives
475 were then combined with finite-strain theory equations (equations 7-23) to evaluate
476 the full elasticity of Fp at high *P*-*T* conditions. We should emphasize that these linear
477 equations can only be used within the solid solution range of approximately 0-20 mol%
478 FeO. Evaluation of the relationship between the elastic moduli and a higher FeO
479 content at high *P*-*T* conditions in the (Mg,Fe)O system will require further
480 experimental data in the future.

481 **FeO effects on the velocity profiles of Fp in the Earth's lower mantle**

This is a preprint, the final version is subject to change, of the American Mineralogist (MSA)
Cite as Authors (Year) Title. American Mineralogist, in press.
DOI: https://doi.org/10.2138/am-2019-6656

The Earth's mantle is generally believed to have a pyrolitic composition (Ringwood 1975). Based on the pyrolite model, Earth's lower mantle consists of approximately 75 vol% Bgm, 20 vol% Fp, and 5 vol% Ca-silicate perovskite (Ca-Pv) (Irifune 1994; Irifune et al. 2010; Ricolleau et al. 2009; Ringwood 1975). Although the exact composition of Earth's lower mantle has yet to be unambiguously determined, the current consensus is that Fp contains approximately 20 mol% FeO, while Bgm contains 10 mol% FeO, together with a few percents of Al_2O_3 in Bgm (e.g., Irifune et al. 2010; Lin et al. 2013; Lin and Tsuchiya 2008; Mattern et al. 2005). The spin transition in both Fp and (Al,Fe)-bearing Bgm can also affect the iron partitioning between these phases (e.g., Irifune et al. 2010; Xu et al. 2017).

To better understand the influence of FeO on the velocity behavior of Fp, we calculated its velocity profiles using the Voigt-Reuss-Hill averages based on our high *P-T* elasticity modeling results for MgO and Fp (Fp10 and Fp20) along an expected mantle geotherm (Katsura et al. 2010) (Fig. 10). These modeled results were then compared with the velocity profiles of Bgm10 (with FeO content of 10 mol%) (Chantel et al. 2012; Murakami et al. 2007), Ca-Pv (Kudo et al. 2012), and the Preliminary Reference Earth Model (PREM) (Dziewonski and Anderson 1981) (Fig. 10). Briefly, the third-order Eulerian finite-strain equations and the third-order Birch-Murnaghan equation of state (Birch 1978) were used to evaluate the K_S and G of the relevant minerals by extrapolating the experimentally-derived elastic moduli and their *P-T* derivatives to relevant *P-T* conditions. The reference *P-T* conditions at 670 km deep were ~23.8 GPa and ~1980 K, and the modeling depth was limited to 1250 km (mid-lower mantle) to avoid the complication of the potential effects of the iron electronic spin transition (e.g., see Lin et al. 2013 for a review).

Our modeled velocity profiles showed that substitution of FeO in Fp could significantly reduce both the V_P and V_S velocities at lower mantle conditions; compared to MgO, the V_P and V_S velocities of Fp20 were reduced by ~8% and ~10 %, respectively. That is, $(\partial V_P/\partial X_{Fe})$ and $(\partial V_S/\partial X_{Fe})$ are approximately -0.04 and -0.03

km/s/X_{Fe}, respectively, in the upper part of the lower mantle. Furthermore, the V_P and V_S velocity profiles of Fp20 are ~8% and ~4% lower than the velocity profiles of the PREM, respectively. On the other hand, Bgm10 has the highest V_P profile and MgO has the highest V_S profile among all lower-mantle minerals, while Fp20 has the lowest V_P profile and Ca-Pv has the lowest V_S profile. The depth-dependent velocity profiles of a volume-weighted pyrolitic aggregate for the Earth's lower mantle, which was obtained from the arithmetic mean aggregation of the compositions (75 vol% Bgm10, 20 vol% Fp20, and 5 vol% Ca-Pv) (Irifune et al. 2010; Ringwood 1975), were extremely consistent with velocity profiles of the PREM within uncertainties.

IMPLICATIONS

Seismic wave anisotropy of Fp in the Earth's lower mantle

Seismic studies of the Earth's mantle have reported seismic anisotropy that could result from the crystallographic lattice preferred orientation (CPO) of the constituent minerals with velocity anisotropy (Blackman and Kendall 2002; Karato et al. 2008; Marquardt and Morales 2012; Marquardt et al. 2009b; Nippress et al. 2004; Niu and Perez 2004; Walpole et al. 2017). The CPO of the constituent minerals could develop due to mantle convection (Boneh and Skemer 2014; Karato 1998; Long and Becker 2010; Mainprice 2015; Tackley 2000). Therefore, understanding the seismic anisotropy of the Earth's lower mantle can greatly help us understand the geodynamics of the deep Earth (Long and Becker 2010; Mainprice et al. 2000; Romanowicz and Wenk 2017). Specifically, the viscosity of Fp seems to be pressure-dependent (Marquardt and Miyagi 2015), but Fp is still among the weakest rheological phases in the lower mantle and can significantly contribute to the seismic anisotropy of the lower mantle (e.g., Immoor et al. 2018; Marquardt et al. 2009b; Miyagi and Wenk 2016). The elastic anisotropy of Fp combined with its rheological weakness can play a significant role in the interpretation of the observed seismic anisotropy in the lower mantle (e.g., Yamazaki and Karato 2001; Yamazaki et al. 2009; Marquardt and Miyagi 2015; Girard et al. 2016).

This is a preprint, the final version is subject to change, of the American Mineralogist (MSA)
Cite as Authors (Year) Title. American Mineralogist, in press.
DOI: https://doi.org/10.2138/am-2019-6656

To decipher the potential influence of Fp on the lower-mantle seismic anisotropy, we calculated the AV_P and AV_S of Fp10 and Fp20 along a representative geotherm using the aforementioned thermoelastic modeling method (Fig. 11). At a 670 km depth, the AV_P and AV_S of Fp20 are 3.7% and 8.86%, respectively, and the difference between the vertically V_{SV} and horizontally V_{SH} polarized shear waves is 0.45 km/s. The AV_P and AV_S of Fp10 are 4.4% and 9.87%, respectively, and the difference between the orthogonally polarized shear waves V_{SV} and V_{SH} is 0.55 km/s. However, at a depth of ~1250 km, the AV_P is 5.0%, AV_S is 11.42% for Fp20, and the difference between V_{SH} and V_{SV} is 0.66 km/s. The AV_P is 3.7% and AV_S is 8.09% for Fp10, and the difference between V_{SH} and V_{SV} is 0.51 km/s. These results showed that Fp was clearly V_P and V_S anisotropic in the upper regions of the lower mantle and both the increase of Fe content in Fp and the increasing depth from 670 km to 1250 km could change the V_P and V_S anisotropies of Fp. We should caution that the extrapolated velocity anisotropies were only for the high-spin Fp, and did not take the potential spin transition effects on the elasticity into account. The spin transition of iron has been reported to significantly enhance the elastic shear anisotropy of Fp at high pressure and room temperature (Marquardt et al. 2009b; Yang et al. 2015), making low-spin Fp much more anisotropic than Bgm (the most abundant lower mantle mineral) in the deeper parts of the lower mantle.

Origins of seismic lateral heterogeneities at the Earth's lower mantle

Seismic lateral heterogeneities have been detected in the lower mantle (e.g., Karato and Karki 2001; Li 2009; Masters et al. 2000; Schumacher et al. 2018; van der Hilst and Kárason 1999; Wu and Wentzcovitch 2017). However, their interpretation is still uncertain. While some studies have suggested that the seismic heterogeneities of the lower mantle was mainly due to thermal effects (e.g., Forte 2000; Forte et al. 1994; Simmons et al. 2010), many other studies have suggested chemically-induced heterogeneities (e.g., Antolik et al. 2003; Garnero and McNamara 2008; Kaneshima and Helffrich 2010; Koelemeijer et al. 2016; Mosca et al. 2012; Resovsky and

Trampert 2003). Distinguishing the thermal or chemical origin of the seismic heterogeneities in the lower mantle is crucial because each origin has a drastically different consequence and affects our understanding of the Earth's interior dynamic (Karato and Karki 2001). Experimental elasticity studies of the major minerals in the lower mantle (such as Fp) at relevant high *P*-*T* conditions play a significant role in understanding the seismic signatures, and also provide a new constraint on the seismic structures and evolution of the lower mantle (Karato and Karki 2001; Yang et al. 2016).

The thermal or chemical origins of the seismic lateral heterogeneities can be constrained by comparing the observed ratios of various seismic parameters with mineral physics results (e.g., Karato and Karki 2001; Wu and Wentzcovitch 2014; Yang et al. 2016). To investigate the thermal variation of the heterogeneities ratios ($R_{S/P}=\partial \ln V_S/\partial \ln V_P$) for Fp, we calculated the thermally-induced variations in V_S and V_P for MgO, Fp10, and Fp20 (Fig. 12a). In the modeling, the velocities of these phases were first extrapolated along a representative geotherm (Katsura et al. 2010) based on the derived thermoelastic parameters and finite-strain theory. In addition, we applied a positive and negative temperature perturbation of 200 K to the velocities to determine the $\partial \ln V_S/\partial T$ and $\partial \ln V_P/\partial T$ for Fp. The $R_{S/P}$ values of MgO, Fp10, and Fp20 show an increase of ~2-5% from 670 km to 1250 km, indicating that high temperature increases the $R_{S/P}$ value of Fp. The $R_{S/P}$ profile of Fp20 is ~ 30% and ~50% higher than Fp10 and MgO, respectively. Therefore, our results showed that the thermally-induced $R_{S/P}$ was sensitive to composition and the FeO content had a significant increasing effect on the thermally-induced $R_{S/P}$ of Fp in the upper part of the lower mantle. This also agrees with a previous theoretical prediction, which showed that compositional variations could change the thermally-induced $R_{S/P}$ depth profiles in the lower mantle (Wu and Wentzcovitch 2017).

The amount of FeO in the Earth's lower mantle minerals is particularly important because it can affect a wide range of elastic properties, including their densities,

This is a preprint, the final version is subject to change, of the American Mineralogist (MSA)
Cite as Authors (Year) Title. American Mineralogist, in press.
DOI: https://doi.org/10.2138/am-2019-6656

sound velocities, bulk and shear moduli (Jacobsen et al. 2002; Yang et al. 2015). Previous studies have also suggested that the variation of FeO content in Fp may be regarded as a potential chemical cause for seismic lateral heterogeneities (van der Hilst and Kárason 1999). Here, we also calculated the Fe-induced variations of V_S and V_P for Fp (MgO, Fp10, and Fp20) from 670 km to 1250 km along a representative geotherm (Fig. 12b). Due to change of the Fe content in Fp, the value of $R_{S/P}$ shows a distinctly increasing trend from ~1.92 at 670 km to ~2.21 at 1250 km (Fig. 12b), which is similar with the upward trending thermally-induced variation of Fp (MgO, Fp10, and Fp20) but has significantly steeper slopes. These results indicate that the value of $R_{S/P}$ distinctly increases with increasing Fe content in Fp. Specifically, the value of $R_{S/P}$ due to change of the Fe content (Fe-induced variation) in Fp is ~ 45% and ~ 20% higher than the thermally-induced variation of MgO and Fp10, respectively. The value of $R_{S/P}$ due to change of the Fe content in Fp is ~ 10% lower than the thermally-induced variation of Fp20. Moreover, our value of $R_{S/P}$ due to change of the Fe content in Fp is also ~ 15% higher than the one from a previous study by Yang et al. (2016) (dot-dashed line in Fig. 12b) within their uncertainties. There are two possible reasons for the slightly different results between this study and Yang et al. (2016). One of them is that we calculated the Fe-induced variations of V_S and V_P for Fp with up to 20 mol% FeO, whereas Yang et al. (2016) only limited Fp with up to 10 mol% FeO. Another reason is that Yang et al. (2016) calculated the relative variations of velocity with a Fe content using the high pressure and room temperature elasticity data of MgO (Sinogeikin and Bass 2000) as their benchmark data. These factors clearly highlight the importance of our current simultaneously high *P*-*T* elasticity studies of MgO.

In addition, even though some seismic studies showed a decreasing trend of $R_{S/P}$ in the upper part of the lower mantle (e.g., Mosca et al. 2012), most seismic studies demonstrated an increasing trend in the same depth region, where the $R_{S/P}$ was ~ 1.7 at the top of the lower mantle and ~2.0 in the mid-lower mantle (e.g., Robertson and

Woodhouse 1996; Romanowicz 2001; Simmons et al. 2010). Compared to the seismic observation results (dashed lines in Fig. 12b), the $R_{S/P}$ value of the thermally-induced variation for Fp10 is consistent with most seismic observations within uncertainty. However, the thermally-induced $R_{S/P}$ value of Fp20, which is the relevant composition of Fp in the lower mantle, is ~50% higher than most seismic observations within uncertainty for the upper part of the lower mantle (e.g., Houser et al. 2008; Kowlemeijer et al. 2016; Mosca et al. 2012; Robertson and Woodhouse 1996; Romanowicz 2001; Simmons et al. 2010). On the contrary, the value of $R_{S/P}$ due to change of the Fe content in Fp is fairly consistent with some seismic observations within uncertainty in the upper part of the lower mantle (e.g., Robertson and Woodhouse 1996; Romanowicz 2001; Simmons et al. 2010). Thus, based on the results for Fp in this study, we propose that the Fe-induced heterogeneities can offer a significant contribution to the observed seismic lateral heterogeneities in the lower mantle. This also agrees with the results of seismology studies, which showed that the seismic heterogeneities in the lower mantle could not be explained by thermal anomalies alone, and suggested the presence of chemical heterogeneities, might be a local variation of Fe content, as an alternative explanation (e.g., Houser et al. 2008; Kellogg et al. 1999; van der Hilst and Kárason 1999; Wysession et al. 1999). We should note that the above mentioned Fe-induced heterogeneities in the lower mantle did not take the potential contributions from Bgm into account because Fe preferentially partitions into Fp in the lower mantle (e.g., Auzende et al. 2008; Kaminsky and Lin 2017; Muir and Brodholt 2016; Sakai et al. 2009; Xu et al. 2017) and there are few single-crystal elasticity experimental studies of Bgm at high *P*-*T* conditions (e.g., Sinogeikin et al. 2004b). Future single-crystal elasticity studies of Fp and Bgm at the relevant *P*-*T* and compositional (the possible Fp and Bgm compositions expected in the lower mantle) conditions are needed to provide a more comprehensive understanding of the seismic anisotropy and lateral heterogeneities of the Earth's lower mantle.

Acknowledgments

We acknowledge Z. Mao, C. Lu and Y. Wu for their constructive suggestions and discussions, and Freyja O'Toole for editing our manuscript. D. W. Fan acknowledges financial support from the National Natural Science Foundation of China (41772043), the Joint Research Fund in Huge Scientific Equipment (U1632112) under the cooperative agreement between NSFC and CAS, CAS "Light of West China" Program (Dawei Fan, 2017), and Youth Innovation Promotion Association CAS (Dawei Fan, 2018434). J. F. Lin acknowledges support form Geophysics and CSEDI Programs of the U.S. National Science Foundation. This work was performed at GeoSoilEnviroCARS (The University of Chicago, Sector 13), Advanced Photon Source (APS), Argonne National Laboratory. GeoSoilEnviroCARS is supported by the National Science Foundation (EAR-0622171) and the Department of Energy (DE-FG02-94ER14466) under Contract No. DE-AC02-06CH11357. This research used resources at the Advanced Photon Source, a U.S. Department of Energy (DOE) Office of Science User Facility operated for the DOE Office of Science by Argonne National Laboratory under Contract No. DE-AC02-06CH11357.

REFERENCES CITED

Andrault, D. (2001) Evaluation of (Mg,Fe) partitioning between silicate perovskite and magnesiowüstite up to 120 GPa and 2300 K. Journal of Geophysical Research, 106(B2), 2079-2087.

Antolik, M., Gu, Y.J., Ekström, G., and Dziewonski, A.M. (2003) J362D28: a new joint model of compressional and shear velocity in the Earth's mantle. Geophysical Journal International, 153(2), 443-466.

Antonangeli, D., Siebert, J., Aracne, C.M., Farber, D.L., Bosak, A., Hoesch, M., Krisch, M., Ryerson, F.J., Fiquet, G., and Badro, J. (2011) Spin crossover in ferropericlase at high pressure: A seismologically transparent transition? Science, 331(6013), 64-67.

Auzende, A.L., Badro, J., Ryerson, F.J., Weber, P.K., Fallon, S.J., Addad, A., Siebert, J., Fiquet, G. (2008) Element partitioning between magnesium silicate perovskite and ferropericlase: New

676 insights into bulk lower-mantle geochemistry. Earth and Planetary Science Letters, 269(1-2),
677 164-174.

678 Badro, J., Fiquet, G., Guyot, F., Rueff, J.P., Struzhkin, V.V., Vanko, G., and Monaco, G. (2003)
679 Iron partitioning in Earth's mantle: Toward a deep lower mantle discontinuity. Science,
680 300(5620), 789-791.

681 Belonoshko, A.B., Arapan, S., Martonak, R., and Rosengren, A. (2010) MgO phase diagram from
682 first principles in a wide pressure-temperature range. Physical Review B, 81(5), 054110.

683 Birch, F. (1978) Finite strain isotherm and velocities for single-crystal and polycrystalline NaCl at
684 high pressure and 300 K. Journal of Geophysical Research, 83(B3), 1257-1268.

685 Blackman, D.K. and Kendall, J.M. (2002) Seismic anisotropy in the upper mantle 2. Predictions
686 for current plate boundary flow models. Geochemistry, Geophysics, Geosystems, 3(9), 8602.

687 Bolis, R.M., Morard, G., Vinci, T., Ravasio, A., Bambrink, E., Guarguaglini, M., Koenig, M.,
688 Musella, R., Remus, F., Bouchet, J., Ozaki, N., Miyanishi, K., Sekine, T., Sano, T., Kodama, R.,
689 Guyot, F., and Benuzzi-Mounaix, A. (2016) Decaying shock studies of phase transitions in
690 MgO-SiO_2 systems: Implications for the super-Earths' interiors. Geophysical Research Letters,
691 43(18), 9475-9483.

692 Boneh, Y., and Skemer, P. (2014) The effect of deformation history on the evolution of olivine
693 CPO. Earth and Planetary Science Letters, 406, 213-222.

694 Chantel, J., Frost, D.J., McCammon, C.A., Jing, Z.C., Wang, Y.B. (2012) Acoustic velocities of
695 pure and iron-bearing magnesium silicate perovskite measured to 25 GPa and 1200 K.
696 Geophysical Research Letters, 39(19), L19307.

697 Chen, G.L., Liebermann, R.C., and Weidner, D.J. (1998) Elasticity of single-crystal MgO to 8
698 gigapascals and 1600 Kelvin. Science, 280(5371), 1913-1916.

699 Coppari, F., Smith, R.F., Eggert, J.H., Wang, J., Rygg, J.R., Lazicki, A., Hawreliak, J.A., Collins,
700 G.W., and Duffy, T.S. (2013) Experimental evidence for a phase transition in magnesium oxide
701 at exoplanet pressures. Nature Geoscience, 6, 926-929.

Crowhurst, J.C., Brown, J.M., Goncharov, A.F., and Jacobsen, S.D. (2008) Elasticity of (Mg,Fe)O Through the Spin Transition of Iron in the Lower Mantle. Science, 319(5862), 451-453.

Dewaele, A., Fiquet, G., Andrault, D., and Hausermann, D. (2000)P-V-T equation of state of periclase from synchrotron radiation measurements. Journal of Geophysical Research, 105(B2), 2869-2877.

Dorfman, S.M., Prakapenka, V.B., Meng, Y., and Duffy, T.S. (2012) Intercomparison of pressure standards (Au, Pt, Mo, MgO, NaCl, and Ne) to 2.5 Mbar. Journal of Geophysical Research, 117(B8), B08210.

Dorogokupets, P.I. (2010) P-V-T equations of state of MgO and thermodynamics. Physics and Chemistry of Minerals, 37(9), 677-684.

Duffy, T.S., and Ahrens, T.J. (1995) Compressional sound velocity, equation of state, and constitutive response of shock-compressed magnesium oxide. Journal of Geophysical Research, 100(B1), 529-542.

Duffy, T.S., and Anderson, D.L. (1989) Seismic velocities in mantle minerals and the mineralogy of the upper mantle. Journal of Geophysical Research, 94(B2), 1895-1912.

Duffy, T.S., Hemley, R.J., Mao, H.K. (1995a) Equation of state and shear strength at multimegabar pressures: Magnesium oxide to 227 GPa. Physical Review Letters, 74(8), 1371-1374.

Duffy, T.S., Madhusudhan, N., and Lee, K.K.M. (2015) Mineralogy of Super-Earth Planets. In: Schubert, G. (eds.) Treatise on Geophysics, 2nd edition, vol. 2, pp.149-178, Oxford: Elsevier.

Duffy, T.S., Zha, C.S., Downs, R.T., Mao, H.K., Hemley, R.J. (1995b) Elasticity of forsterite to 16 GPa and the composition of the upper mantle. Nature, 378, 170-173.

Dziewonski, A.M., and Anderson, D.L. (1981) Preliminary reference Earth model. Physics of the Earth and Planetary Interiors, 25(4), 297-356.

Every, A. (1980) General closed-form expressions for acoustic waves in elastically anisotropic solids. Physical Review B, 22(4), 1746.

728 Fan, D.W., Mao, Z., Yang, J., Lin, J.F. (2015) Determination of the full elastic tensor of single
729 crystals using shear wave velocities by Brillouin spectroscopy. American Mineralogist,
730 100(11-12), 2590-2601.

731 Fei, Y.W. (1999) Effects of temperature and composition on the bulk modulus of (Mg,Fe)O.
732 American Mineralogist, 84(3), 272-276.

733 Fei, Y.W., Ricolleau, A., Frank, M., Mibe, K., Shen, G.Y., and Prakapenka, V.B. (2007) Towards
734 an internally consistent pressure scale. Proceedings of the National Academy of Sciences,
735 104(22), 9182-9186.

736 Fiquet, G., Badro, J., Guyot, F., Bellin, Ch., Krisch, M., Antonangeli, D., Requardt, H., Mermet,
737 A., Farber, D., Aracne-Ruddle, C., Zhang, J. (2004) Application of inelastic X-ray scattering to
738 the measurements of acoustic wave velocities in geophysical materials at very high pressure.
739 Physics of the Earth and Planetary Interiors, 143-144, 5-18.

740 Forte, A.M. (2000) Seismic-geodynamic constraints on mantle flow: Implications for layered
741 convection, mantle viscosity, and seismic anisotropy in the deep mantle. In: Karato, S.I., Forte,
742 A., Liebermann, R.C., Masters, G., and Stixrude, L. (eds.), Earth's Deep Interior: Mineral
743 Physics and Tomography from the Atomic to the Global Scale, Geophysical Monograph Series,
744 vol. 177, pp. 441-477, American Geophysical Union, Washington, DC.

745 Forte, A.M., Woodward, R.L., and Dziewonski, A.M. (1994) Joint inversions of seismic and
746 geodynamic data for models of three-dimensional mantle heterogeneities. Journal of
747 Geophysical Research, 99(B11), 21857-21877.

748 Fu, S.Y., Yang, J., and Lin, J.F. (2017) Abnormal elasticity of single-crystal magnesiosiderite
749 across the spin transition in Earth's lower mantle. Physical Review Letters, 118(3), 036402.

750 Garnero, E.J., and McNamara, A.K. (2008) Structure and dynamics of Earth's lower mantle.
751 Science, 320(5876), 626-628.

752 Girard, J., Amulele, G., Farla, R., Mohiuddin, A., Karato, S.-I. (2016) Shear deformation of
753 bridgmanite and magnesiowüstite aggregates at lower mantle conditions. Science, 351(6269),
754 144-147.

755 Grimsditch, M. (2001) Brillouin scattering. In: Levy, M., Bass, H., Stern, R., Keppens, V. (eds.),
756 Handbook of Elastic Properties of Solids, Liquids, and Gases. pp. 331-347, Academic Press.

757 Hager, B.H., Clayton, R.W., Richards, M.A., Comer, R.P., and Dziewonski, A.M. (1984) Lower
758 mantle heterogeneities, dynamic topography and the geoid. Nature, 313(14), 541-545.

759 Hill, R. (1952) The elastic behaviour of a crystalline aggregate. Proceedings of the Physical
760 Society-Section A, 65(5), 349-354.

761 Houser, C., Masters, G., Shearer, P., and Laske, G. (2008) Shear and compressional velocity
762 models of the mantle from cluster analysis of long-period waveforms. Geophysical Journal
763 International, 174(1), 195-212.

764 Immoor, J., Marquardt, H., Miyagi, L., Lin, F., Speziale, S., Merkel, S., Buchen, J., Kurnosov, A.,
765 Liermann, H.-P. (2018) Evidence for {100}<011> slip in ferropericlase in Earth's lower mantle
766 from high-pressure/high-temperature experiments. Earth and Planetary Science Letters, 489,
767 251-257.

768 Irifune, T. (1994) Absence of an aluminous phase in the upper part of the Earth's lower mantle.
769 Nature, 370, 131-133.

770 Irifune, T., Shinmei, T., McCammon, C.A., Miyaljima, N., Rubie, D.C., and Frost, D.J. (2010)
771 Iron partitioning and density changes of pyrolite in Earth's lower mantle. Science, 327(5962),
772 193-195.

773 Isaak, D.G., Anderson, O.L., and Goto, T. (1989) Measured elastic moduli of single-crystal MgO
774 up to 1800 K. Physics and Chemistry of Minerals, 16(7), 704-713.

775 Isaak, D.G., Cohen, R.E., and Mehl, M.J. (1990) Calculated elastic and thermal properties of MgO
776 at high pressures and temperatures. Journal of Geophysical Research, 95(B5), 7055-7067.

777 Ito, E., Kubo, A., Katsura, T., and Walter, M.J. (2004) Melting experiments of mantle materials
778 under lower mantle conditions with implications for magma ocean differentiation. Physics of
779 the Earth and Planetary Interiors, 143-144, 397-406.

780 Jackson, I., and Niesler, H. (1982) The elasticity of periclase to 3 GPa and some geophysical
781 implications. In: Akimoto, S., and Manghnani, M.H. (eds.), High Pressure Research in
782 Geophysics, pp. 93-113, Center for Academic Publications Japan, Tokyo.

783 Jackson, J.M., Sinogeikin, S.V., Jacobsen, S.D., Reichmann, H.J., Mackwell, S.J., and Bass, J.D.
784 (2006) Single-crystal elasticity and sound velocities of $(Mg_{0.94}Fe_{0.06})O$ ferropericlase to 20 GPa.
785 Journal of Geophysical Research, 111(B9), B09203.

786 Jacobsen, S.D., Reichmann, H.J., Spetzler, H.A., Mackwell, S.J., Smyth, J.R., Angel, R.J., and
787 McCammon, C.A. (2002) Structure and elasticity of single-crystal (Mg,Fe)O and a new method
788 of generating shear waves for gigahertz ultrasonic interferometry. Journal of Geophysical
789 Research, 107(B2), ECV 4-1-ECV 4-14.

790 Jacobsen, S.D., Spetzler, H., Reichmann, H.J., and Smyth, J.R. (2004) Shear waves in the
791 diamond-anvil cell reveal pressure-induced instability in (Mg,Fe)O. Proceedings of the National
792 Academy of Sciences, 101(16), 5867-5871.

793 Jacobsen, S.D., Holl, C.M., Adams, K.A., Fischer, R.A., Martin, E.S., Bina, C.R., Lin, J.F.,
794 Prakapenka, V.B., Kubo, A., and Dera, P. (2008) Compression of single-crystal magnesium
795 oxide to 118 GPa and a ruby pressure gauge for helium pressure media. American Mineralogist,
796 93(11-12), 1823-1828.

797 Kaminsky, F.V., and Lin, J.F. (2017) Iron partitioning in natural lower-mantle minerals: Toward a
798 chemically heterogeneous lower mantle. American Mineralogist, 102(4), 824-832.

799 Kaneshima, S., and Helffrich, G. (2010) Small scale heterogeneities in the mid-lower mantle
800 beneath the circum-Pacific area. Physics of the Earth and Planetary Interiors, 183(1), 91-103.

801 Kantor, I., Prakapenka, V., Kantor, A., Dera, P., Kurnosov, A., Sinogeikin, S., Dubrovinskaia, N.,
802 and Dubrovinsky, L. (2012) BX90: A new diamond anvil cell design for X-ray diffraction and
803 optical measurements. Review of Scientific Instruments, 83(12), 125102.

804 Karato, S.I. (1998) Seismic anisotropy in the deep mantle, boundary layers and the geometry of
805 mantle convection. Pure and Applied Geophysics, 151(2-4), 565-587.

806 Karato, S.I., Jung, H., Katayama, I., and Skmer, P. (2008) Geodynamic significance of seismic
807 anisotropy of the upper mantle: New insights from laboratory studies. Annual Review of Earth
808 and Planetary Sciences, 36, 59-95.

809 Karato, S., and Karki, B.B. (2001) Origin of lateral variation of seismic wave velocities and
810 density in the deep mantle. Journal of Geophysical Research, 106(B10), 21771-21783.

811 Karki, B.B., Stixrude, L., Clark, S.J., Warren, M.C., Ackland, G.J., and Crain, J. (1997) Structure
812 and elasticity of MgO at high pressure. American Mineralogist, 82(1-2), 51-60.

813 Karki, B.B., Wentzcovitch, R.M., Gironcoli, S., and Baroni, S. (1999) First-principles
814 determination of elastic anisotropy and wave velocities of MgO at lower mantle conditions.
815 Science, 286(5445), 1705-1707.

816 Katsura, T., Yoneda, A., Yamazaki, D., Yoshino, T., Ito, E. (2010) Adiabatic temperature profile
817 in the mantle. Physics of the Earth and Planetary Interiors, 183(1-2), 212-218.

818 Kellogg, L.H., Hager, B.H., and van der Hilst, R.D. (1999) Compositional stratification in the
819 deep mantle. Science, 283(5409), 1881-1884.

820 Kimura, T., Ohfuji, H., Nishi, M., and Irifune, T. (2017) Melting temperature of MgO under high
821 pressure by micro-texture analysis. Nature Communications, 8, 15735.

822 Koelemeijer, P., Ritsema, J., Deuss, A., and van Heijst, H.-J. (2016) SP12RTS: A degree-12
823 model of shear-and compressional-wave velocity for Earth's mantle. Geophysical Journal
824 International, 204(2), 1024-1039.

825 Kono, Y., Irifune, T., Higo, Y., Inoue, T., and Barnhoorn, A. (2010) P-V-T relation of MgO
826 derived by simultaneous elastic wave velocity and in situ X-ray measurements: A new pressure

827 scale for the mantle transition region. Physics of the Earth and Planetary Interiors, 183(1-2),
828 196-211.

829 Kudo, Y., Hirose, K., Murakami, M., Asahara, Y., Ozawa, H., Ohishi, Y., and Hirao, N. (2012)
830 Sound velocity measurements of $CaSiO_3$ perovskite to 133 GPa and implications for lowermost
831 mantle seismic anomalies. Earth and Planetary Science Letters, 349-350, 1-7.

832 Kung, J., Li, B.S., Weidner, D.J., Zhang, J.Z., and Liebermann, R.C. (2002) Elasticity of
833 $(Mg_{0.83},Fe_{0.17})O$ ferropericlase at high pressure: ultrasonic measurements in conjunction with
834 X-radiation techniques. Earth and Planetary Science Letters, 203(1), 557-566.

835 Li, B.S. (2009) Characteristics of lateral heterogeneities with thermal and chemical origins in the
836 pyrolitic lower mantle. Progress in Natural Science, 19(11), 1603-1611.

837 Li, B.S., Woody, K., and Kung, J. (2006), Elasticity of MgO to 11 GPa with an independent
838 absolute pressure scale: Implications for pressure calibration. Journal of Geophysical Research,
839 111(B11), B11206.

840 Li, B., Kung, J., Uchida, T., and Wang, Y.B. (2005) Pressure calibration to 20 GPa by
841 simultaneous use of ultrasonic and x-ray techniques. Journal of Applied Physics, 98(1), 013521.

842 Lin, J.F., Struzhkin, V.V., Jacobsen, S.D., Hu, M.Y., Chow, P., Kung, J., Liu, H., Mao, H.K., and
843 Hemley, R.J. (2005) Spin transition of iron in magnesiowustite in the Earth's lower mantle.
844 Nature, 436(7049), 377-380.

845 Lin, J.F., Jacobsen, S.D., Sturhahn, W., Jackson, J.M., Zhao, J.C., and Yoo, C.S. (2006) Sound
846 velocities of ferropericlase in the Earth's lower mantle. Geophysical Research Letters, 33(22),
847 L22304.

848 Lin, J.F., Speziale, S., Mao, Z., and Marquardt, H. (2013) Effects of the electronic spin transitions
849 of iron in lower-mantle minerals: Implications to deep-mantle geophysics and geochemistry.
850 Reviews of Geophysics, 51(2), 244-275.

851 Lin, J.F., and Tsuchiya, T. (2008) Spin transition of iron in the Earth's lower mantle. Physics of
852 the Earth and Planetary Interiors, 170(3-4), 248-259.

853 Long, M.D., and Becker, T.W. (2010) Mantle dynamics and seismic anisotropy. Earth and
854 Planetary Science Letters, 297, 341-354.

855 Lu, C., Mao, Z., Lin, J.F., Zhuravlev, K.K., Tkachev, S.N., and Prakapenka, V.B. (2013) Elasticity
856 of single-crystal iron-bearing pyrope up to 20 GPa and 750 K. Earth and Planetary Science
857 Letters, 361, 134-142.

858 Mainprice, D. (1990) A Fortran Program to Calculate Seismic Anisotropy from the Lattice
859 Preferred Orientation of Minerals. Computers & Geosciences, 16(3), 385-393.

860 Mainprice, D. (2015) Seismic Anisotropy of the Deep Earth from a Mineral and Rock Physics
861 Perspective. In: Schubert, G. (eds.), Treatise on Geophysics, 2nd edition, vol 2, pp. 487-538,
862 Oxford: Elsevier.

863 Mainprice, D., Barruol, G., and Ben Ismail, W. (2000) The anisotropy of the Earth's mantle: From
864 single crystal to polycrystal. In: Karato, S.I., Stixrude, L., Liebermann, R., Masters, G., and
865 Forte, A. (eds.), Mineral Physics and Seismic Tomography from the Atomic to the Global Scale,
866 Geophysical Monograph Series, vol. 177, pp. 237-264, American Geophysical Union,
867 Washington, DC.

868 Mao, H.K., Xu, J., and Bell, P.M. (1986) Calibration of the ruby pressure gauge to 800 kbar under
869 quasi-hydrostatic conditions. Journal of Geophysical Research, 91(B5), 4673-4676.

870 Mao, H.K., Shen, G.Y., and Hemley, R.J. (1997) Multivariable dependence of Fe-Mg partitioning
871 in the lower mantle. Science, 278(5346), 2098-2100.

872 Mao, Z., Fan, D.W., Lin, J.F., Yang, J., Tkachev, S.N., Zhuravlev, K., and Prakapenka, V.B.
873 (2015) Elasticity of single-crystal olivine at high pressures and temperatures. Earth and
874 Planetary Science Letters, 426, 204-215.

875 Mao, Z., Lin, J.F., Jacobsen, S.D., Duffy, T.S., Chang, Y.Y., Smyth, J.R., Frost, D.J., Hauri, E.H.,
876 and Prakapenka, V.B. (2012) Sound velocities of hydrous ringwoodite to 16 GPa and 673 K.
877 Earth and Planetary Science Letters, 331-332, 112-119.

878 Marquardt, H., and Miyagi, L. (2015) Slab stagnation in the shallow lower mantle linked to an
879 increase in mantle viscosity. Nature Geoscience, 8(4), 311-314.

880 Marquardt, H., and Morales, L. (2012) Ferropericlase layering as potential cause for seismic
881 anisotropy in Earth's lower mantle? European Mineralogical Conference, 1, EMC2012-562.

882 Marquardt, H., Speziale, S., Reichmann, H.J., Frost, D.J., and Schilling, F.R. (2009a)
883 Single-crystal elasticity of $(Mg_{0.9}Fe_{0.1})O$ to 81 GPa. Earth and Planetary Science Letters,
884 287(3-4), 345-352.

885 Marquardt, H., Speziale, S., Reichmann, H.J., Frost, D.J., Schilling, F.R., and Garnero, E.J.
886 (2009b) Elastic shear anisotropy of ferropericlase in Earth's lower mantle. Science, 324(5924),
887 224-226.

888 Masters, G., Laske, G., Bolton, H., and Dziewonski, A. (2000) The relative behavior of shear
889 velocity, bulk sound speed, and compressional velocity in the mantle: Implications for chemical
890 and thermal structure. In: Karato, S.I., Stixrude, L., Liebermann, R., Masters, G., and Forte, A.
891 (eds.), Mineral Physics and Seismic Tomography from the Atomic to the Global Scale,
892 Geophysical Monograph Series, vol. 177, pp. 63-87, American Geophysical Union, Washington,
893 DC.

894 Matsui, M., Parker, S.C., and Leslie, M. (2000) The MD simulation of the equation of state of
895 MgO: Application as a pressure calibration standard at high temperature and high pressure.
896 American Mineralogist, 85(2), 312-316.

897 Mattern, E., Matas, J., Ricard, Y., Bass, J.D. (2005) Lower mantle composition and temperature
898 from mineral physics and thermodynamic modeling. Geophysical Journal International, 160(3),
899 973–990.

900 McWilliams, R.S., Spaulding, D.K., Eggert, J.H., Celliers, P.M., Hicks, D.G., Smith, R.F., Collins,
901 G.W., and Jeanloz, R. (2012) Phase transformations and metallization of magnesium oxide at
902 high pressure and temperature. Science, 338(6112), 1330-1333.

Miyagi, L., and Wenk, H.-R. (2016) Texture development and slip systems in bridgmanite and bridgmanite+ferropericlase aggregates. Physics and Chemistry of Minerals, 43(8), 597-613.

Mosca, I., Cobden, L., Deuss, A., Ritsema, J., and Trampert, J. (2012) Seismic and mineralogical structures of the lower mantle from probabilistic tomography. Journal of Geophysical Research, 117(B6), B06304.

Muir, J.M.R., and Brodholt, J.P. (2015) Elastic properties of ferropericlase at lower mantle conditions and its relevance to ULVZs. Earth and Planetary Science Letters, 417, 40-48.

Muir, J.M.R., and Brodholt, J.P. (2016) Ferrous iron partitioning in the lower mantle. Physics of the Earth and Planetary Interiors, 257, 12-17.

Murakami, M., Ohishi, Y., Hirao, N., and Hirose, K. (2009) Elasticity of MgO to 130 GPa: Implications for lower mantle mineralogy. Earth and Planetary Science Letters, 277(1-2), 123-129.

Murakami, M., Ohishi, Y., Hirao, N., and Hirose, K. (2012) A perovskitic lower mantle inferred from high-pressure, high-temperature sound velocity data. Nature, 485(7396), 90-94.

Murakami, M., Sinogeikin, S.V., Hellwig, H., Bass, J.D., and Li, J. (2007) Sound velocity of $MgSiO_3$ perovskite to Mbar pressure. Earth and Planetary Science Letters, 256(1-2), 47-54.

Nippress, S.E.J., Kusznir, N.J., and Kendall, J.M. (2004) Modeling of lower mantle seismic anisotropy beneath subduction zones. Geophysical Research Letters, 31(19), L19612.

Niu, F.L., and Perez, A.M. (2004) Seismic anisotropy in the lower mantle: A comparison of waveform splitting of SKS and SKKS. Geophysical Research Letters, 31(24), L24612.

Oganov, A.R., Gillan, M.J., Price, G.D. (2003) Ab initio lattice dynamics and structural stability of MgO. The Journal of Chemical Physics, 118(22), 10174-10182.

Ostwald, J., Pazold, W., and Weis, O. (1977) High-resolution Brillouin spectroscopy of water. Applied Physics, 13(4), 351-356.

Polian, A., Vo-Thanh, D., and Richet, P. (2002) Elastic properties of α-SiO_2 up to 2300 K from Brillouin scattering measurements. Europhysics Letters, 57(3), 375-381.

929 Reichmann, H.J., Angel, R.J., Spetzler, H., and Bassett, W.A. (1998) Ultrasonic interferometry
930 and X-ray measurements on MgO in a new diamond anvil cell. American Mineralogist,
931 83(11-12), 1357-1360.

932 Reichmann, H.J., Sinogeikin, S.V., and Bass, J.D. (2008) Single-crystal elastic properties of
933 $(Mg_{0.987},Fe_{0.013})O$ to 9 GPa. American Mineralogist, 93(8-9), 1306-1311.

934 Resovsky, J., and Trampert, J. (2003) Using probabilistic seismic tomography to test mantle
935 velocity–density relationships. Earth and Planetary Science Letters, 215(1-2), 121-134.

936 Ricolleau, A., Fei, Y.W., Cottrell, E., Watson, H., Deng, L.W., Zhang, L., Fiquet, G., Auzende,
937 A.-L., Roskosz, M., Morard, G., and Prakapenka, V. (2009) Density profile of pyrolite under
938 the lower mantle conditions. Geophysical Research Letters, 36(6), L06302.

939 Ringwood, A.E. (1975) Composition and Petrology of the Earth's Mantle. McGraw-Hill, New
940 York.

941 Robertson, G.S., and Woodhouse, J.H. (1996) Ratio of relative S to P velocity heterogeneities in
942 the lower mantle. Journal of Geophysical Research, 101(B9), 20041-20052.

943 Romanowicz, B. (2001) Can we resolve 3D density heterogeneities in the lower mantle?
944 Geophysical Research Letters, 28(6), 1107-1110.

945 Romanowicz, B., and Wenk, H.-R.(2017) Anisotropy in the deep Earth. Physics of the Earth and
946 Planetary Interiors, 269, 58-90.

947 Sakai, T., Ohtani, E., Terasaki, H., Sawada, N., Kobayashi, Y., Miyahara, M., Nishijima, M.,
948 Hirao, N., Ohishi, Y., Kikegawa, T. (2009) Fe-Mg partitioning between perovskite and
949 ferropericlase in the lower mantle. American Mineralogist, 94(7), 921-925.

950 Sandercock, J.R. (1982) Trends in Brillouin scattering: studies of opaque materials, supported
951 films, and central modes. In: Cardona, M., and Guntherodt, J. (eds.), Topics in Applied Physics,
952 pp. 173-206, Springer-Verlag, Berlino.

953 Sang, L.Q., and Bass, J.D. (2014) Single-crystal elasticity of diopside to 14 GPa by Brillouin
954 scattering. Physics of the Earth and Planetary Interiors, 228, 75-79.

955 Schumacher, L., Thomas, C., and Abreu, R. (2018) Out-of-Plane seismic reflections beneath the
956 Pacific and their geophysical implications. Journal of Geophysical Research, 123(3),
957 2286-2302.

958 Simmons, N. A., Forte, A. M., Boschi, L., and Grand, S. P. (2010) GyPSuM: A joint tomographic
959 model of mantle density and seismic wave speeds. Journal of Geophysical Research, 115(B12),
960 B12310.

961 Sinogeikin, S.V., and Bass, J.D. (2000) Single-crystal elasticity of pyrope and MgO to 20 GPa by
962 Brillouin scattering in the diamond cell. Physics of the Earth and Planetary Interiors, 120(1-2),
963 43-62.

964 Sinogeikin, S.V., and Bass, J.D. (2002) Elasticity of majorite and a majorite-pyrope solid solution
965 to high pressure: implications for the transition zone. Geophysical Research Letters, 29(2),
966 1017.

967 Sinogeikin, S.V., Bass, J.D., Prakapenka, V., Lakshtanov, D., Shen, G., Sanchez-Valle, C., and
968 Rivers, M. (2006) Brillouin spectrometer interfaced with synchrotron radiation for simultaneous
969 X-ray density and acoustic velocity measurements. Review of Scientific Instruments, 77(10),
970 103905.

971 Sinogeikin, S.V., Jackson, J.M., O'Neill, B., Palko, J.W., and Bass, J.D. (2000) Compact
972 high-temperature cell for Brillouin scattering measurements. Review of Scientific Instruments,
973 71(1), 201-206.

974 Sinogeikin, S.V., Lakshtanov, D.L., Nicholas, J.D., and Bass, J.D. (2004a) Sound velocity
975 measurements on laser-heated MgO and Al_2O_3. Physics of the Earth and Planetary Interiors,
976 143-144, 575-586.

977 Sinogeikin, S.V, Zhang, J.Z., and Bass, J.D. (2004b) Elasticity of single crystal and
978 polycrystalline $MgSiO_3$ perovskite by Brillouin spectroscopy. Geophysical Research Letters,
979 31(6), L06620.

980 Speziale, S. Marquardt, H., Duffy, T.S. (2014) Brillouin Scattering and its Application in
981 Geosciences. Reviews in Mineralogy & Geochemistry, 78(1), 543-603.

982 Speziale, S., Zha, C.S., Duffy, T.S., Hemley, R.J., and Mao, H.K. (2001) Quasi-hydrostatic
983 compression of magnesium oxide to 52 GPa: Implications for the pressure-volume-temperature
984 equation of state. Journal of Geophysical Research, 106(B1), 515-528.

985 Sumino, Y., Anderson, O.L., and Suzuki, I. (1983) Temperature coefficients of elastic constants of
986 single crystal MgO between 80 and 1300 K. Physics and Chemistry of Minerals, 9(1), 38-47.

987 Tackley, P.J. (2000) Mantle convection and plate tectonics: Toward an integrated physical and
988 chemical theory. Science, 288(5473), 2002-2007.

989 Tange, Y., Nishihara, Y., and Tsuchiya, T. (2009) Unified analyses for P-V-T equation of state of
990 MgO: A solution for pressure-scale problems in high P-T experiments. Journal of Geophysical
991 Research, 114(B3), B03208.

992 Tateno, S., Hirose, K., and Ohishi, Y. (2014) Melting experiments on peridotite to lowermost
993 mantle conditions. Journal of Geophysical Research, 119(6), 4684-4694.

994 Tsuchiya, T., Wentzcovitch, R.M., da Silva, C.R.S., and de Gironcoli, S.(2006) Spin transition in
995 magnesiowustite in Earth's lower mantle. Physical Review Letters, 96(19), 198501.

996 Utsumi, W., Weidner, D.J., and Lieberman, R.C. (1998) Volume measurement of MgO at high
997 pressures and temperatures. In: Manghnani, M.H. and Yagi, T. (eds.) Properties of earth and
998 planetary materials at high pressure and temperature, Geophysical Monograph Series, vol. 101,
999 pp 327-333, American Geophysical Union, Washington, DC.

1000 van der Hilst, R.D., and Kárason, H. (1999) Compositional heterogeneities in the bottom 1000
1001 kilometers of Earth's mantle: Toward a hybrid convection model. Science, 283(5409),
1002 1885-1888.

1003 Walpole, J., Wookey, J., Kendall, J.M., and Masters, T.G. (2017) Seismic anisotropy and mantle
1004 flow below subducting slabs. Earth and Planetary Science Letters, 465, 155-167.

1005 Wentzcovitch, R.M., Justo, J.F., Wu, Z.Q., da Silva, C.R.S., Yuen, D.A., and Kohlstedt, D. (2009)
1006 Anomalous compressibility of ferropericlase throughout the iron spin cross-over. Proceedings
1007 of the National Academy of Sciences, 106(21), 8447-8452.

1008 Wood, B.J. (2000) Phase transformations and partitioning relations in peridotite under lower
1009 mantle conditions. Earth and Planetary Science Letters, 174(3-4), 341-354.

1010 Wu, Y., Yang, J., Wu, X., Song, M.S., Yoshino, T., Zhai, S.M., Qin, S., Huang, H.J., and Lin, J.F.
1011 (2016) Elasticity of single-crystal NAL phase at high pressure: A potential source of the seismic
1012 anisotropy in the lower mantle. Journal of Geophysical Research, 121(8), 5696-5707.

1013 Wu, Z.Q., Justo, J.F., da Silva, C.R.S., de Gironcoli, S., Wentzcovitch, R.M. (2009) Anomalous
1014 thermodynamic properties in ferropericlase throughout its spin crossover. Physical Review B,
1015 80(1), 014409.

1016 Wu, Z.Q., and Wentzcovitch, R. M. (2014) Spin crossover in ferropericlase and velocity
1017 heterogeneities in the lower mantle. Proceedings of the National Academy of Sciences, 111(29),
1018 10468-10472.

1019 Wu, Z.Q., and Wentzcovitch, R.M. (2017) Composition versus temperature induced velocity
1020 heterogeneities in a pyrolitic lower mantle. Earth and Planetary Science Letters, 457, 359-365.

1021 Wu, Z.Q., Wentzcovitch, R.M., Umemoto, K., Li, B.S., Hirose, K., and Zheng, J.C. (2008)
1022 Pressure-volume-temperature relations in MgO: An ultrahigh pressure-temperature scale for
1023 planetary sciences applications. Journal of Geophysical Research, 113(B6), B06204.

1024 Wysession, M.E., Langenhorst, A., Fouch, M.J., Fischer, K.M., Al-Eqabi, G.I., Shore, P.J., and
1025 Clarke, T.J. (1999) Lateral variations in compressional/shear velocities at the base of the mantle.
1026 Science, 284(5411), 120-125.

1027 Xu, S.Z., Lin, J.F., and Morgan, D. (2017) Iron partitioning between ferropericlase and
1028 bridgmanite in the Earth's lower mantle. Journal of Geophysical Research, 122(2), 1074-1087.

1029 Yamazaki, D., and Karato, S. (2001) Some mineral physics constraints on the rheology and
1030 geothermal structure of Earth's lower mantle. American Mineralogist, 86(4), 385-391.

Yamazaki, D., Yoshino, T., Matsuzaki, T., Katsura, T., Yoneda, A. (2009) Texture of (Mg,Fe)SiO_3perovskite and ferro-periclase aggregate: implications for rheology of the lower mantle. Physics of the Earth and Planetary Interiors, 174(1-4), 138-144.

Yang, J., Lin, J.F., Jacobsen, S.D., Seymour, N.M., Tkachev, S.N., and Prakapenka, V.B. (2016) Elasticity of ferropericlase and seismic heterogeneities in the Earth's lower mantle. Journal of Geophysical Research, 121(12), 8488-8500.

Yang, J., Mao, Z., Lin, J.F., and Prakapenka, V.B. (2014) Single-crystal elasticity of the deep-mantle magnesite at high pressure and temperature. Earth and Planetary Science Letters, 392, 292-299.

Yang, J., Tong, X.Y., Lin, J.F., Okuchi, T., and Tomioka, N. (2015) Elasticity of ferropericlase across the spin crossover in the Earth's lower mantle. Scientific Reports, 5, 17188.

Yoneda, A. (1990) Pressure derivatives of elastic constants of single crystal MgO and $MgAl_2O_4$. Journal of Physics of the Earth, 38(1), 19-55.

Zerr, A., and Boehler, R. (1994) Constraints on the melting temperature of the lower mantle from high-pressure experiments on MgO and magnesiowüstite. Nature, 371(), 506-508.

Zha, C.S., Mao, H.K., and Hemley, R.J. (2000) Elasticity of MgO and a primary pressure scale to 55 GPa. Proceedings of the National Academy of Sciences, 97(25), 13494-13499.

Zhang, J.S., and Bass, J.D. (2016) Sound velocities of olivine at high pressures and temperatures and the composition of Earth’s upper mantle. Geophysical Research Letters, 43(18), 9611-9618.

Figure Captions

Figure 1. Representative sample chamber image and X-ray diffraction image along the principal crystallographic axis [100] of single-crystal MgO platelet at high *P-T* conditions. (a) MgO (100) platelet, together with Au and a ruby sphere calibrant, in Ne medium; (b) Representative X-ray diffraction pattern along the principal crystallographic axis [100] of single-crystal MgO platelet at 11.65 GPa and 700 K. The inset shows the high-quality single crystal nature with a typical FWHM of a diffraction peak of MgO at ±0.2°. (Color online.)

Figure 2. Representative Brillouin spectra of single-crystal periclase MgO at high pressure and temperature. Open circles: experimental data; solid lines: fitted V_P and V_S peaks, respectively. (Color online.)

Figure 3. Pressure-volume-temperature relations of single-crystal periclase MgO. The results are derived from analysis of X-ray diffraction measurements in EHDACs. Solid symbols represent experimental data at 300 K, 500 K, 700 K, and 900 K. Solid lines are fits to experimental data using the third-order Birch-Murnaghan equation of state. The inset shows the density of MgO as a function of pressure at the given high temperatures. (Color online.)

Figure 4. Acoustic velocities of the single-crystal periclase MgO along the [110] and [100] crystallographic directions as a function of pressure and temperature. Solid circles: experimental data; solid lines: modeled results using the finite-strain theory. (Color online.)

Figure 5. Single-crystal elastic moduli of periclase MgO as a function of pressure and temperature. Solid lines are the fitted results using the third-order finite-strain equation. (Color online.)

This is a preprint, the final version is subject to change, of the American Mineralogist (MSA)
Cite as Authors (Year) Title. American Mineralogist, in press.
DOI: https://doi.org/10.2138/am-2019-6656

Figure 6. Aggregate elastic moduli and velocities of periclase MgO as a function of pressure and temperature. Solid lines are fits to the experimental data using the third-order finite-strain equation. (Color online.)

Figure 7. Upper hemisphere pole figures of V_P anisotropy and V_S splitting anisotropy of single-crystal periclase MgO at representative pressures and temperatures. Calculations were performed using the petrophysical software UnicefCareware of Mainprice (1990) with the derived single-crystal elastic moduli from this study. (Color online.)

Figure 8. Single-crystal elastic moduli of ferropericlase (Mg,Fe)O as a function of the FeO content at ambient conditions. Solid symbols are experimental Brillouin light scattering results for MgO (this study), Fp1 (Reichmann et al. 2008), Fp6 (Yang et al. 2016), and Fp10 (Marquardt et al. 2009). Solid lines are linear fits to the Brillouin experimental data. Black dashed lines: ultrasonic results at ambient conditions by Jacobsen et al. (2002) for comparison. (Color online.)

Figure 9. Pressure and temperature derivatives of the single-crystal elastic moduli of ferropericlase (Mg,Fe)O as a function of the FeO content at high *P*-*T* conditions. Solid symbols are derived from experimental Brillouin results for MgO (this study), Fp6 (Yang et al. 2016), and Fp10 (Marquardt et al. 2009). Solid lines are linear fits to the Brillouin experimental data. (Color online.)

Figure 10. Aggregate V_P and V_S of bridgmanite, ferropericlase, and Ca-perovskite in the Earth's lower mantle. These results are compared with the PREM model (Dziewonski and Anderson 1981). For the pyrolite mineralogical model, we used 75 vol% Bgm10 (Chantel et al. 2012; Murakami et al. 2007), 20 vol% Fp20 (This study),

and 5 vol% Ca-Pv (Kudo et al. 2012). Red line: Fp20; magenta lines: Fp10; cyan lines: MgO; blue lines: Bgm10; green lines: Ca-Pv; and crosses: PREM. Error bars represent the propagated uncertainties (±1σ). (Color online.)

Figure 11. Upper hemisphere pole figures of the V_P anisotropy and V_S splitting anisotropy of Fp10 and Fp20 at 670 and 1250 km, respectively. Calculations were performed using the petrophysical software UnicefCareware of Mainprice (1990) with the modeled single-crystal elastic moduli from this study. (Color online.)

Figure 12. Depth profile of the thermally-induced (a) and Fe-induced (b) heterogeneities ratios ($R_{S/P}=\partial \ln V_S/\partial \ln V_P$) for Fp along a representative geotherm (Katsura et al. 2010). (a) Solid blue line: thermal-induced heterogeneities ratio of MgO; solid green line: thermal-induced heterogeneities ratio of Fp10; solid red line: thermal-induced heterogeneities ratio of Fp20; (b) Solid black line: Fe-induced heterogeneities ratio of Fp; and orange dot-dashed line: Fe-induced heterogeneities ratio of Fp6 (Yang et al. 2016). Seismic models are also shown as a dashed line. Magenta dashed line: SP12RTS (Koelemeijer et al. 2016); cyan dashed line: HMSL08 (Houser et al. 2008); wine dashed line: MCDRT12 (Mosca et al. 2012); red dashed line: GyPSuM (Simmons et al. 2010); blue dashed line: RW96 (Robertson and Woodhouse 1996); and green dashed line: RB01 (Romanowicz 2001). The representative error bars (standard deviation, ±1σ) are estimated using the standard error propagation from the modeled parameters. Vertical lines with arrows represent the differences in percentage for the $R_{S/P}$ ratios. (Color online.)

This is a preprint, the final version is subject to change, of the American Mineralogist (MSA)
Cite as Authors (Year) Title. American Mineralogist, in press.
DOI: https://doi.org/10.2138/am-2019-6656

Table 1 Unit cell volume, adiabatic bulk modulus, and shear modulus of MgO at high *P*-*T*

T(K)	*P*(GPa)	*V* (Å^3)	*V*/*V*$_0$	*K*$_S$(GPa)	*G*(GPa)
300	1.34(2)	74.10(4)	0.9918	168(1)	133(3)
	3.01(2)	73.37(2)	0.9821	174(2)	137(3)
	3.72(4)	73.07(5)	0.9780	177(2)	139(2)
	6.71(3)	71.87(2)	0.9620	188(2)	145(2)
	8.68(5)	71.13(5)	0.9521	195(1)	149(3)
	11.97(4)	69.97(3)	0.9366	207(2)	156(2)
	15.56(5)	68.80(3)	0.9209	219(2)	163(2)
	18.36(5)	67.95(4)	0.9095	229(2)	168(2)
	21.18(6)	67.14(3)	0.8987	239(2)	174(3)
500	2.89(2)	73.90(2)	0.9892	169(2)	133(3)
	4.95(2)	73.01(4)	0.9772	176(2)	137(3)
	7.17(2)	72.11(3)	0.9652	184(2)	142(3)
	9.56(3)	71.20(3)	0.9530	193(2)	147(3)
	11.53(2)	70.49(4)	0.9435	201(2)	151(3)
	13.69(4)	69.75(4)	0.9336	209(2)	156(3)
	15.33(3)	69.21(5)	0.9264	214(2)	159(3)
	17.30(5)	68.59(2)	0.9181	221(2)	163(3)
	18.15(4)	68.33(3)	0.9146	224(2)	164(3)
	20.03(4)	67.77(4)	0.9071	231(2)	168(3)
	22.42(5)	67.09(4)	0.8980	239(2)	173(3)
	24.92(6)	66.41(5)	0.8889	248(2)	177(3)
	26.61(4)	65.97(4)	0.8830	254(2)	181(3)
700	6.32(2)	72.95(3)	0.9764	177(1)	136(2)

This is a preprint, the final version is subject to change, of the American Mineralogist (MSA)
Cite as Authors (Year) Title. American Mineralogist, in press.
DOI: https://doi.org/10.2138/am-2019-6656

	9.11(3)	71.83(2)	0.9615	187(2)	142(3)
	11.65(3)	70.88(3)	0.9487	195(2)	147(2)
	14.33(3)	69.94(4)	0.9362	205(2)	153(3)
	16.82(4)	69.12(4)	0.9252	212(2)	157(3)
	17.90(3)	68.78(5)	0.9206	217(2)	159(3)
	19.89(5)	68.17(2)	0.9125	225(2)	164(3)
	22.60(4)	67.38(4)	0.9019	235(2)	169(3)
	24.18(5)	66.94(3)	0.8960	242(2)	173(3)
	26.80(5)	66.29(5)	0.8873	248(2)	177(3)
	28.14(6)	65.89(4)	0.8819	255(2)	180(3)
900	6.75(2)	73.31(2)	0.9813	172(2)	132(2)
	9.66(3)	72.11(4)	0.9652	182(2)	138(3)
	11.88(3)	71.26(3)	0.9538	190(2)	143(3)
	14.75(4)	70.23(3)	0.9400	200(2)	149(3)
	18.15(5)	69.10(4)	0.9249	212(2)	156(3)
	22.45(5)	67.79(5)	0.9074	227(2)	164(3)
	26.01(4)	66.79(3)	0.8940	241(2)	172(3)
	29.63(5)	65.84(4)	0.8813	254(2)	178(3)

This is a preprint, the final version is subject to change, of the American Mineralogist (MSA)
Cite as Authors (Year) Title. American Mineralogist, in press.
DOI: https://doi.org/10.2138/am-2019-6656

Table 2 Densities, sound velocities of MgO along the [100] and [110] directions, and elastic moduli as a function of pressure at 300 K, 500 K, 700 K, and 900 K

P (MgO) (GPa)	Density (g/cm^3)	V_S[100] (km/s)	V_P[100] (km/s)	V_S[110] (km/s)	V_P[110] (km/s)	C_{11} (GPa)	C_{12} (GPa)	C_{44} (GPa)
				300 K				
1.34(2)	3.608(2)	6.559(7)	9.2(1)	5.391(7)	9.96(1)	308(1)	97.8(7)	155(2)
3.01(2)	3.644(3)	6.558(8)	9.4(1)	5.543(7)	10.05(2)	324(1)	99.6(9)	157(1)
3.72(4)	3.659(5)	6.567(6)	9.5(1)	5.585(8)	10.09(2)	329(1)	101(1)	158(1)
6.71(3)	3.720(3)	6.554(7)	9.8(2)	5.812(8)	10.23(2)	355(2)	104(1)	160(2)
8.68(5)	3.759(5)	6.559(9)	9.9(2)	5.931(7)	10.32(2)	371(2)	107(1)	162(2)
11.97(4)	3.821(4)	6.577(9)	10.2(1)	6.124(9)	10.49(2)	399(2)	112(1)	165(2)
15.56(5)	3.886(6)	6.579(8)	10.5(2)	6.324(7)	10.63(2)	426(2)	115(1)	168(1)
18.36(5)	3.935(5)	6.59(1)	10.7(2)	6.464(8)	10.75(2)	448(2)	120(1)	171(1)
21.18(6)	3.982(3)	6.61(1)	10.9(2)	6.612(9)	10.88(2)	471(2)	123(1)	174(1)
				500 K				
2.89(2)	3.618(2)	6.550(8)	9.2(1)	5.383(9)	9.96(2)	308(2)	98.7(8)	155(1)
4.95(2)	3.662(2)	6.554(8)	9.4(1)	5.532(8)	10.07(2)	326(2)	102(1)	157(2)
7.17(2)	3.708(3)	6.544(7)	9.6(2)	5.673(8)	10.16(2)	344(2)	105(1)	159(1)
9.56(3)	3.755(2)	6.542(9)	9.9(2)	5.849(9)	10.28(2)	364(2)	107(1)	161(2)
11.53(2)	3.793(3)	6.551(8)	10.0(1)	5.969(7)	10.38(2)	381(2)	111(1)	163(2)
13.69(4)	3.833(3)	6.57(1)	10.2(2)	6.120(7)	10.50(2)	400 (2)	113(1)	166(2)
15.33(3)	3.863(4)	6.57(1)	10.3(2)	6.186(8)	10.55(2)	411 (2)	116(1)	167(2)
17.30(5)	3.898(3)	6.573(9)	10.5(2)	6.307(9)	10.64(2)	428(2)	118(2)	168(2)
18.15(4)	3.913(5)	6.58(1)	10.5(2)	6.334(7)	10.67(2)	433(2)	119(1)	169(1)
20.03(4)	3.945(6)	6.59(1)	10.7(2)	6.452(9)	10.76(2)	450(2)	121(1)	171(1)

22.42(5)	3.985(5)	6.60(1)	10.8(1)	6.57(1)	10.86(2)	468(2)	125(1)	173(2)
24.92(6)	4.026(4)	6.608(9)	11.0(2)	6.69(1)	10.96(2)	488(2)	128(1)	176(2)
26.61(4)	4.053(4)	6.62(1)	11.1(2)	6.77(1)	11.04(2)	502(2)	130(1)	178(2)
				700 K				
6.32(2)	3.665(2)	6.549(9)	9.4(1)	5.466(8)	10.05(2)	323(2)	104(1)	157(1)
9.11(3)	3.722(3)	6.534(8)	9.6(2)	5.660(8)	10.18(2)	346(2)	107(1)	159(2)
11.65(3)	3.772(3)	6.53(1)	9.8(2)	5.814(9)	10.28(2)	365(2)	110(1)	161(1)
14.33(3)	3.823(2)	6.546(9)	10.1(1)	5.990(9)	10.41(2)	388(2)	113(1)	164(2)
16.82(4)	3.868(2)	6.549(7)	10.2(2)	6.094(7)	10.49(2)	404(2)	116(1)	166(2)
17.90(3)	3.887(3)	6.549(9)	10.3(2)	6.17(1)	10.55(2)	414(2)	118(1)	167(2)
19.89(5)	3.922(4)	6.57(1)	10.5(2)	6.33(1)	10.67(2)	435(2)	121(1)	169(1)
22.60(4)	3.968(3)	6.57(1)	10.7(2)	6.461(9)	10.78(3)	455(2)	124(1)	171(2)
24.18(5)	3.994(3)	6.60(1)	10.9(2)	6.573(8)	10.88(3)	472(2)	127(1)	174(2)
26.80(5)	4.033(4)	6.60(1)	11.0(2)	6.64(1)	10.94(2)	485(2)	129(1)	176(2)
28.14(6)	4.058(5)	6.61(1)	11.1(2)	6.74(1)	11.03(2)	501(2)	132(1)	177(2)
				900 K				
6.75(2)	3.647(2)	6.532(9)	9.2(1)	5.33(1)	9.96(2)	310(2)	103(1)	156(2)
9.66(3)	3.708(3)	6.53(1)	9.5(2)	5.53(1)	10.10(2)	334(2)	107(1)	158(2)
11.88(3)	3.752(3)	6.524(9)	9.7(2)	5.667(9)	10.19(3)	350(2)	109(1)	160(2)
14.75(4)	3.807(4)	6.525(9)	9.9(1)	5.85(1)	10.32(3)	374(2)	113(1)	162(2)
18.15(5)	3.869(5)	6.54(1)	10.2(2)	6.04(1)	10.48(3)	400(2)	118(1)	166(1)
22.45(5)	3.944(5)	6.55(1)	10.5(2)	6.29(1)	10.66(3)	435(2)	123(2)	169(2)
26.01(4)	4.003(4)	6.58(1)	10.8(2)	6.500(9)	10.84(3)	467(2)	128(1)	173(2)
29.63(5)	4.061(3)	6.59(1)	11.0(2)	6.67(1)	10.98(3)	494(2)	133(2)	176(2)

This is a preprint, the final version is subject to change, of the American Mineralogist (MSA)
Cite as Authors (Year) Title. American Mineralogist, in press.
DOI: https://doi.org/10.2138/am-2019-6656

Table 3 Single-crystal elastic moduli and their pressure and temperature derivatives of MgO at ambient conditions

Study	Methods [a]	C_{11} (GPa)	C_{12} (GPa)	C_{44} (GPa)	$(\partial C_{11}/\partial P)_{300K}$	$(\partial C_{12}/\partial P)_{300K}$	$(\partial C_{44}/\partial P)_{300K}$	$(\partial C_{11}/\partial T)_P$ (GPa/K)	$(\partial C_{12}/\partial T)_P$ (GPa/K)	$(\partial C_{44}/\partial T)_P$ (GPa/K)
This study	BLS	297.9(6)	95.1(5)	152.8(4)	8.35(5)	1.46(2)	1.26(3)	-0.062(3)	0.001(2)	-0.010(2)
Sinogeikin and Bass (2000)	BLS	298(2)	96(1)	154(2)	9.1(2)	1.3(2)	0.8(2)	—[b]	—[b]	—[b]
Sinogeikin et al. (2000)	BLS	—[b]	—[b]	—[b]	—[b]	—[b]	—[b]	-0.060(2)	0.001(1)	-0.015(1)
Zha et al. (2000)	BLS	297.0(1)	95.2(7)	155.7(5)	—[b]	—[b]	—[b]	—[b]	—[b]	—[b]
Jackson and Niesler (1982)	UI	296.8[c]	95.3[c]	155.8[c]	9.17[c]	1.61[c]	1.11[c]	—[b]	—[b]	—[b]
Yoneda (1990)	UI	297.8[c]	95.1[c]	155.8(2)	8.76[c]	1.81[c]	1.31[c]	—[b]	—[b]	—[b]
Sumino et al. (1983)	RPR	297(1)	96(1)	156.2(3)	—[b]	—[b]	—[b]	-0.0596[c]	0.0068[c]	-0.0122(2)
Isaak et al. (1989)	RPR	299.0(7)	96.4(6)	157.1(3)	—[b]	—[b]	—[b]	-0.0585[c]	0.0075[c]	-0.0126[c]
Karki et al. (1999)	DFT	300[c]	94[c]	147[c]	—[b]	—[b]	—[b]	-0.0598[c]	0.0089[c]	-0.0088[c]

[a)] BLS: Brillouin Light Scattering; UI: Ultrasonic Interferometer; RPR: Rectangular Parallelepiped Resonance; and DFT: Density Functional Theory.

[b)] The value is not available in the text.

[c)] The uncertainty is not available in the text.

This is a preprint, the final version is subject to change, of the American Mineralogist (MSA)
Cite as Authors (Year) Title. American Mineralogist, in press.
DOI: https://doi.org/10.2138/am-2019-6656

Table 4 Bulk and shear moduli and their pressure and temperature derivatives of MgO at ambient conditions

References	Methods [a]	K_{S0} (GPa)	G_0 (GPa)	$(\partial K_S/\partial P)_{300K}$	$(\partial G/\partial P)_{300K}$	$(\partial K_S/\partial T)_P$ (GPa/K)	$(\partial G/\partial T)_P$ (GPa/K)
This study	BLS	162.8(2)	130.3(2)	3.94(5)	2.17(2)	-0.025(1)	-0.020(1)
Sinogeikin and Bass (2000)	BLS	163(1)	130(1)	4.0(1)	2.4(1)	—[b]	—[b]
Sinogeikin et al. (2000)	BLS	—[b]	—[b]	—[b]	—[b]	-0.019(2)	-0.024(2)
Zha et al. (2000)	BLS	162.5(7)	130(2)	3.99(3)	2.85(9)	—[b]	—[b]
Murakami et al. (2009)	BLS	—[b]	130(3)	—[b]	1.9(1)	—[b]	—[b]
Murakami et al. (2012)	BLS	—[b]	—[b]	—[b]	—[b]	—[b]	-0.020(1)
Kono et al. (2010)	UI	162.0(4)	128.5(2)	4.27(3)	2.33(1)	-0.0184(4)	-0.0226(2)
Li et al. (2006)	UI	164(1)	129.8(6)	4.2(1)	2.42(6)	—[b]	—[b]
Yoneda (1990)	UI	162.7(2)	131.1[c]	4.1(3)	2.41[c]	—[b]	—[b]
Jackson and Niesler (1982)	UI	162.5(2)	130.9[c]	4.13(9)	2.53[c]	—[b]	—[b]
Sumino et al. (1983)	RPR	163(1)	133.9(2)	—[b]	—[b]	-0.018(2)	-0.021(1)
Isaak et al. (1989)	RPR	163.9(6)	131.8(5)	—[b]	—[b]	-0.0145[c]	-0.024[c]
Karki et al. (1997)	PP	159.7[c]	121.5[c]	4.26[c]	2.18[c]	—[b]	—[b]
Karki et al. (1999)	DFT	162[c]	128[c]	4.15[c]	2.44[c]	-0.014[c]	-0.0216[c]
Matsui et al. (2000)	MD	161[c]	131[c]	4.1[c]	2.4[c]	-0.028[c]	-0.024[c]

[a)] PP: Pseudopotential; and MD: Molecular Dynamic.

[b)] The value is not available in the text.

[c)] The uncertainty is not available in the text.

This is a preprint, the final version is subject to change, of the American Mineralogist (MSA)
Cite as Authors (Year) Title. American Mineralogist, in press.
DOI: https://doi.org/10.2138/am-2019-6656

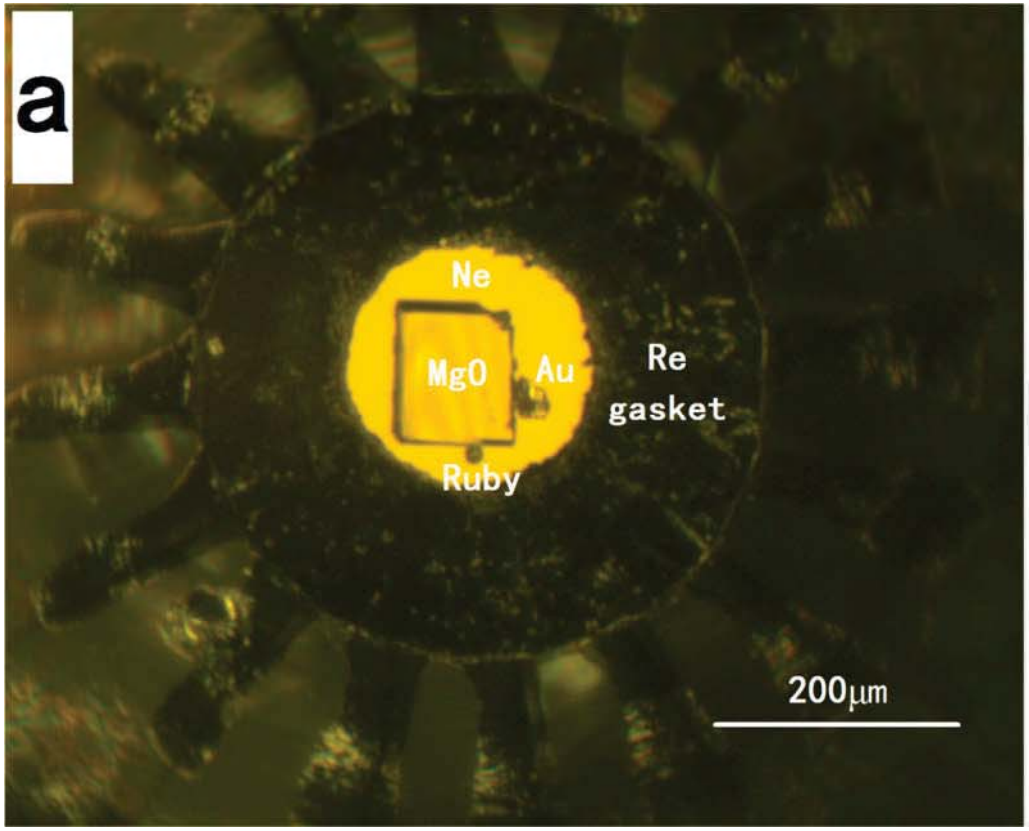

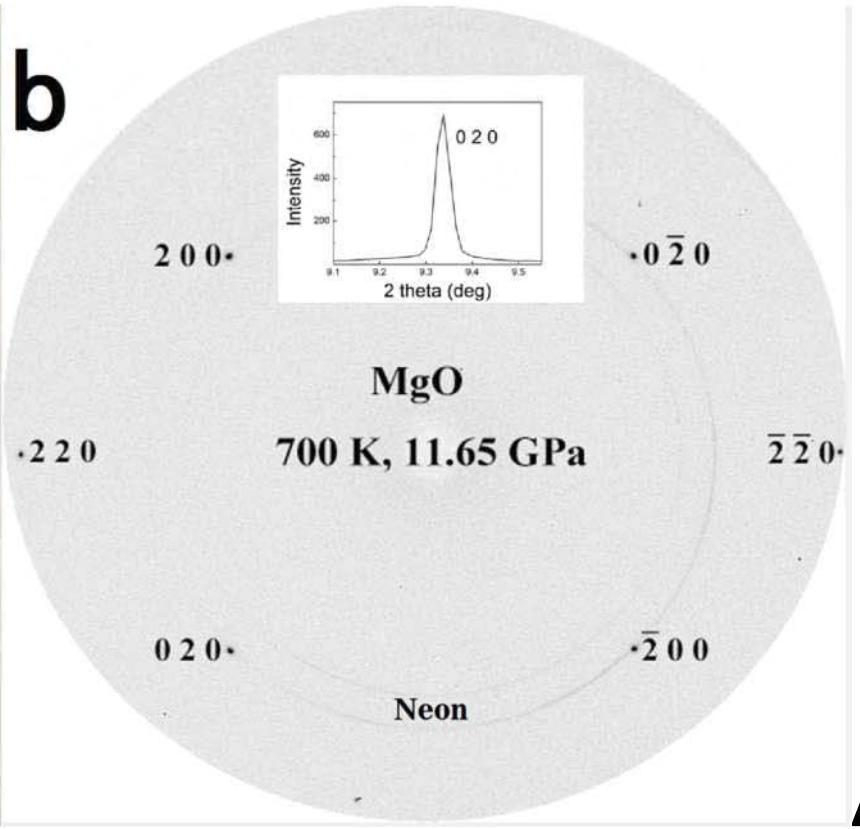

This is a preprint, the final version is subject to change, of the American Mineralogist (MSA)
Cite as Authors (Year) Title. American Mineralogist, in press.
DOI: https://doi.org/10.2138/am-2019-6656

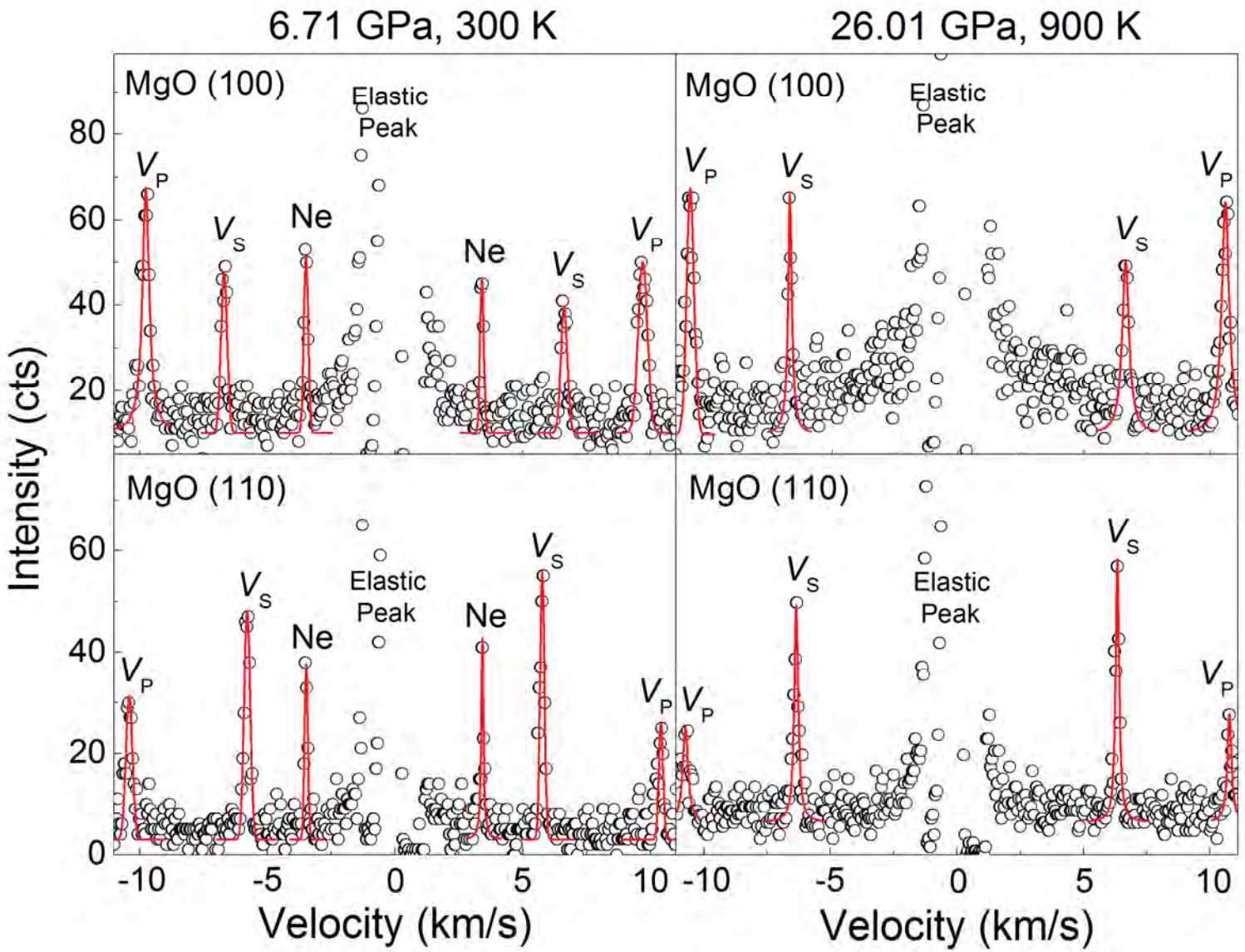

Ā

À !"Ā$Ā

This is a preprint, the final version is subject to change, of the American Mineralogist (MSA)
Cite as Authors (Year) Title. American Mineralogist, in press.
DOI: https://doi.org/10.2138/am-2019-6656

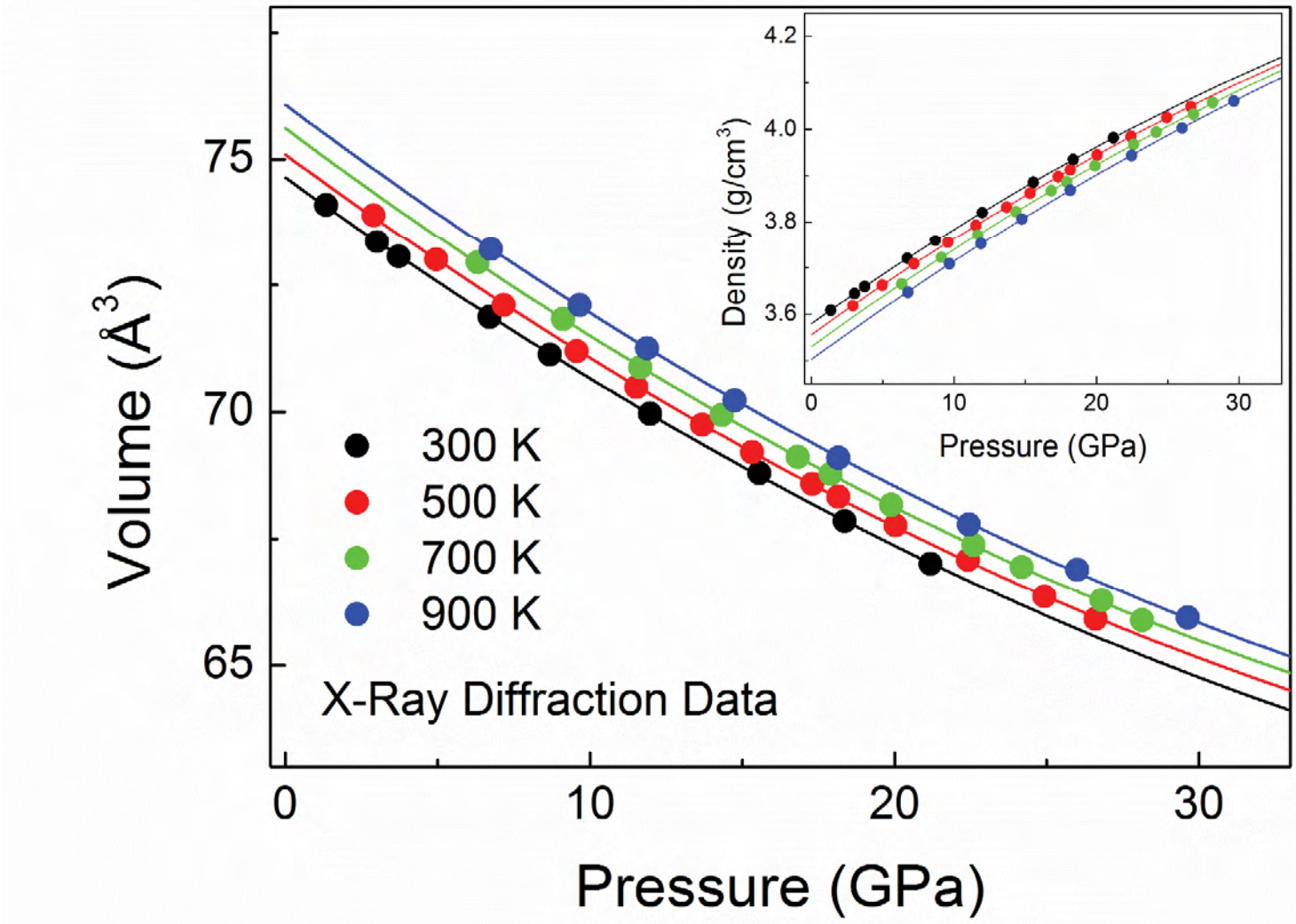

Ā

À !"Ā%Ā

This is a preprint, the final version is subject to change, of the American Mineralogist (MSA)
Cite as Authors (Year) Title. American Mineralogist, in press.
DOI: https://doi.org/10.2138/am-2019-6656

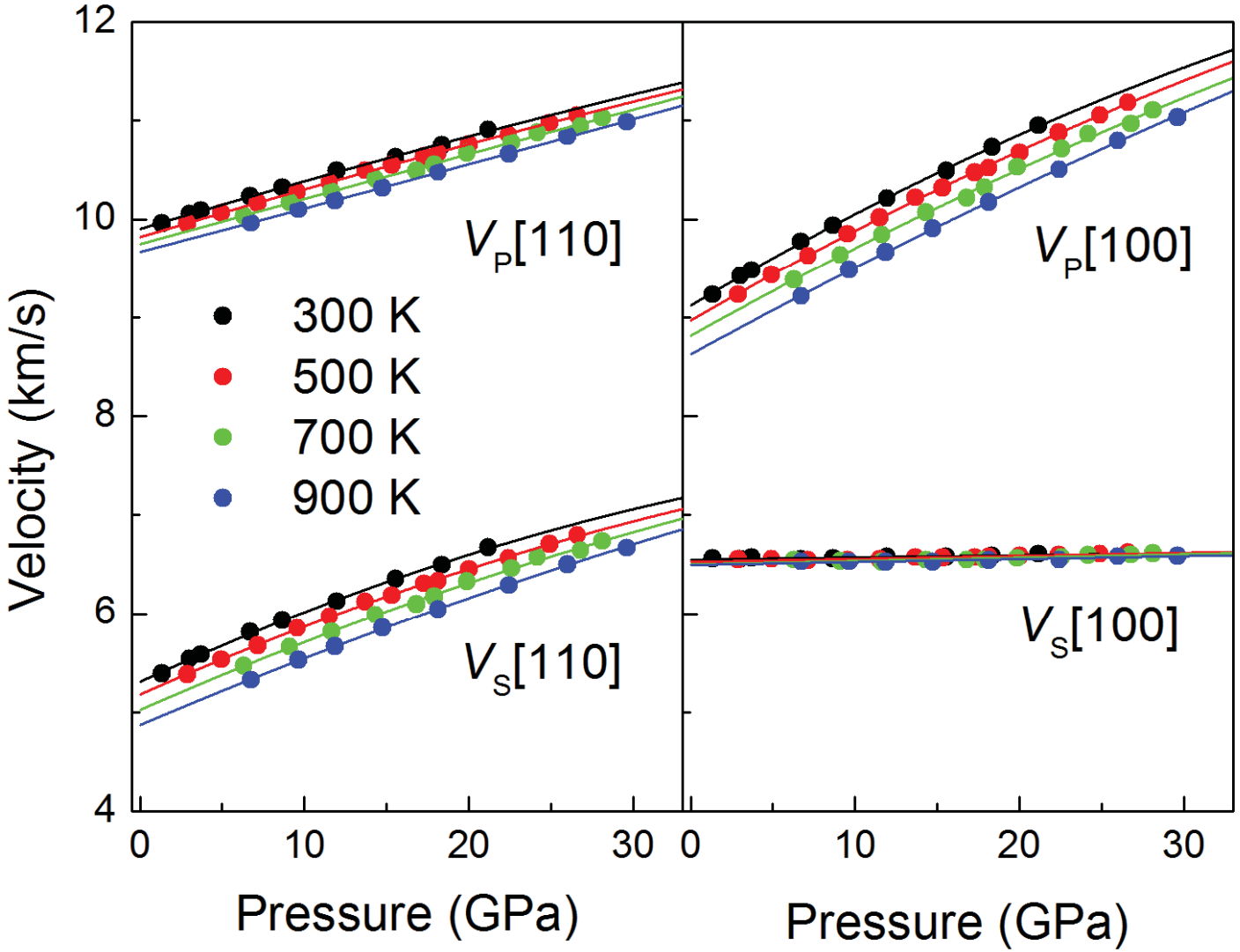

Ā

Ā

Ā

À !"Ā&Ā

This is a preprint, the final version is subject to change, of the American Mineralogist (MSA)
Cite as Authors (Year) Title. American Mineralogist, in press.
DOI: https://doi.org/10.2138/am-2019-6656

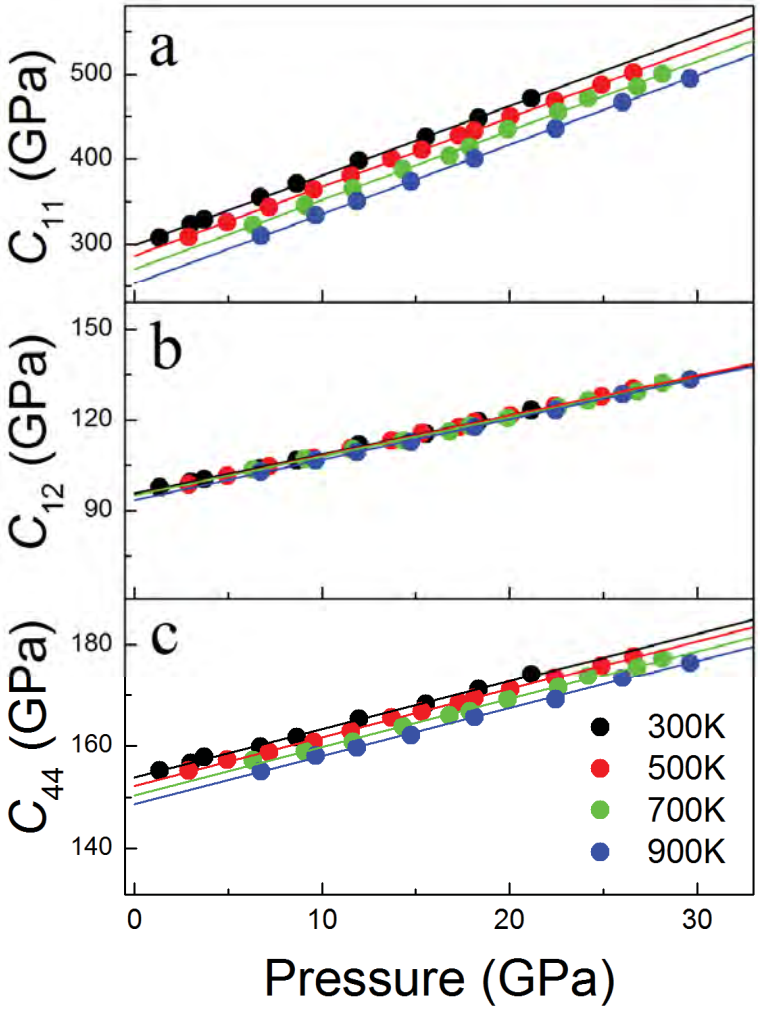

Ā

À !"Ā'Ā

This is a preprint, the final version is subject to change, of the American Mineralogist (MSA)
Cite as Authors (Year) Title. American Mineralogist, in press.
DOI: https://doi.org/10.2138/am-2019-6656

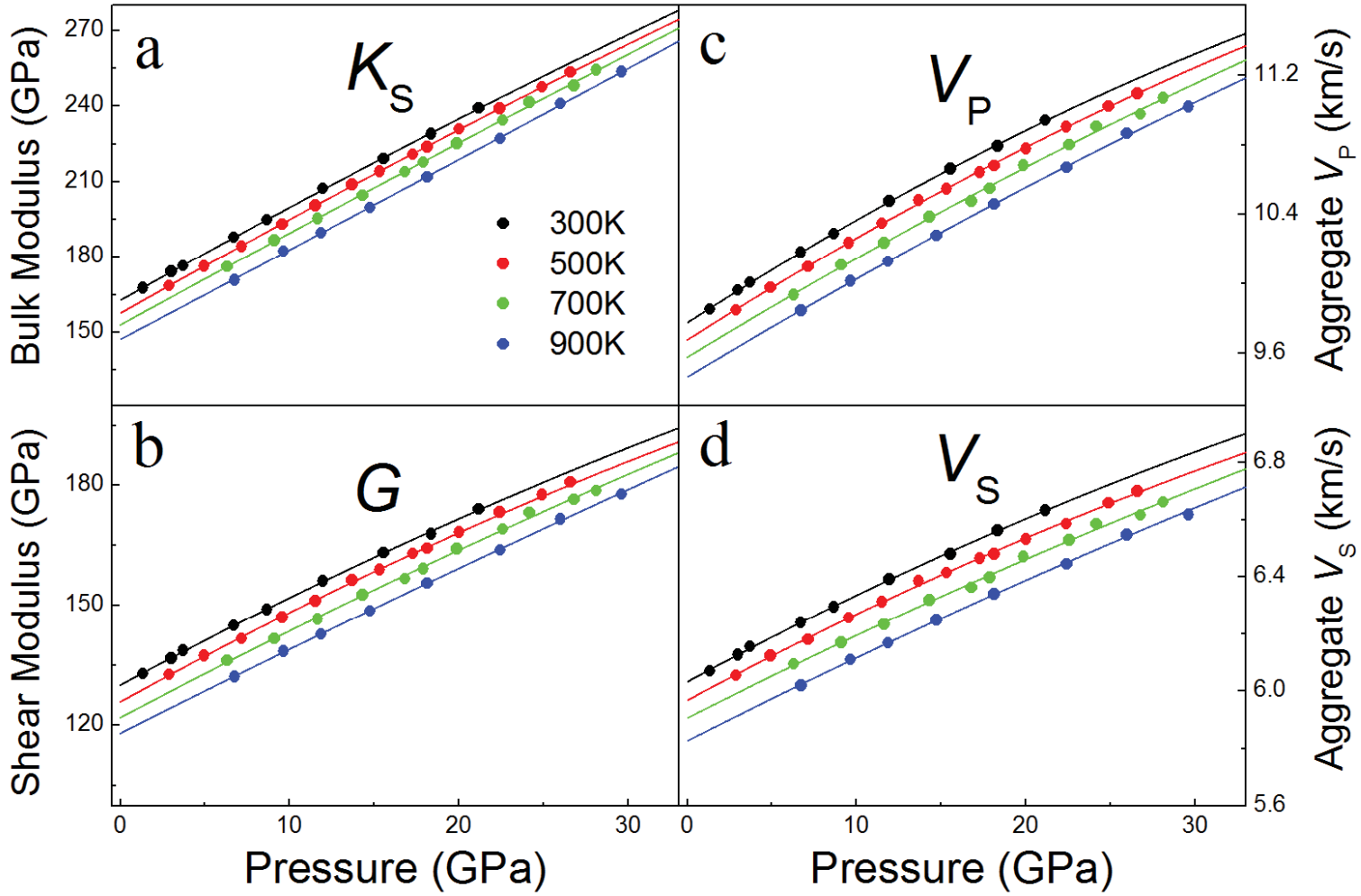

Ā

Ä !"Ā(Ā

DOI: https://doi.org/10.2138/am-2019-6656

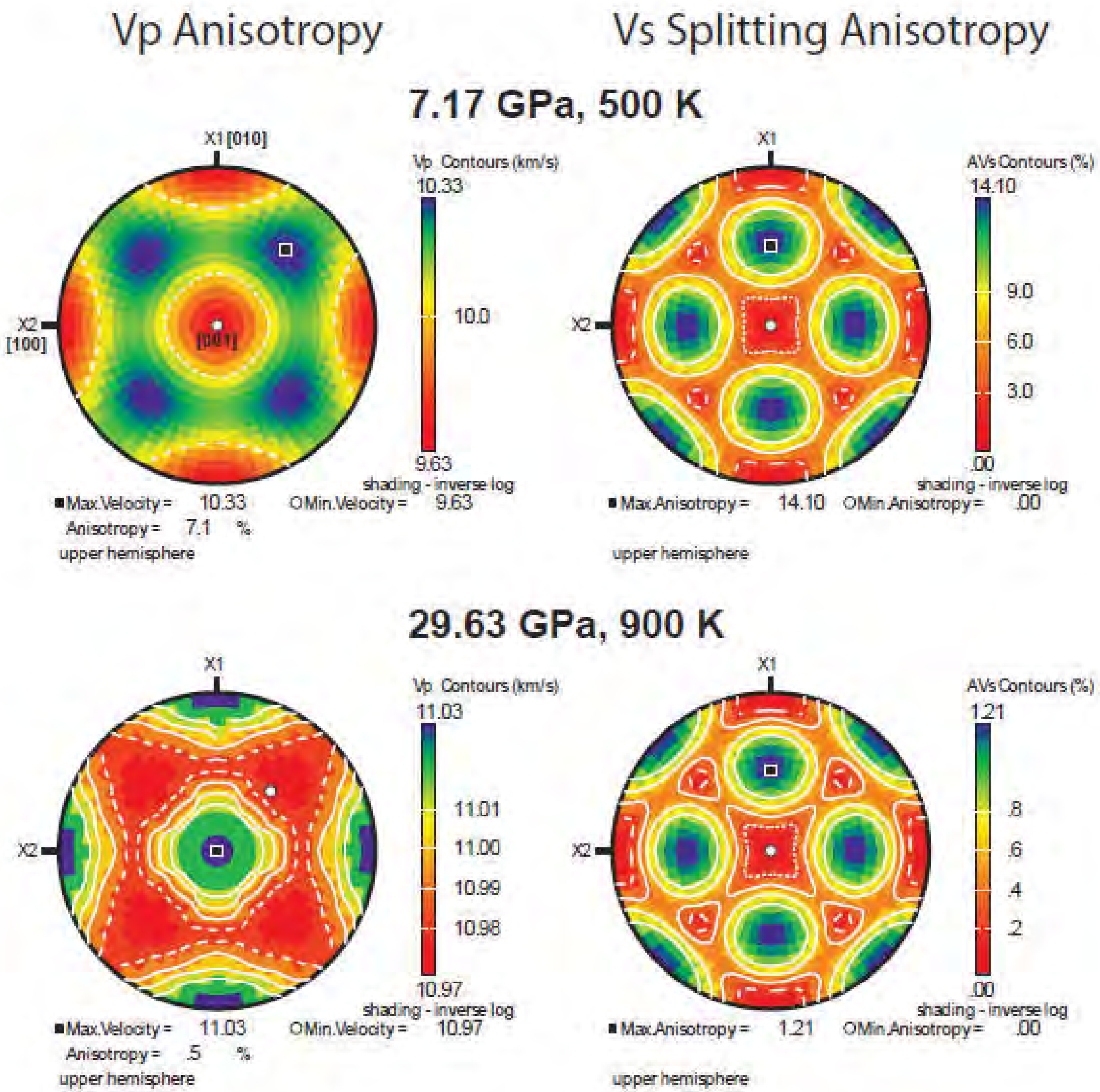

Ā

ĀĀĀĀĀĀĀĀĀĀĀĀĀ

This is a preprint, the final version is subject to change, of the American Mineralogist (MSA)
Cite as Authors (Year) Title. American Mineralogist, in press.
DOI: https://doi.org/10.2138/am-2019-6656

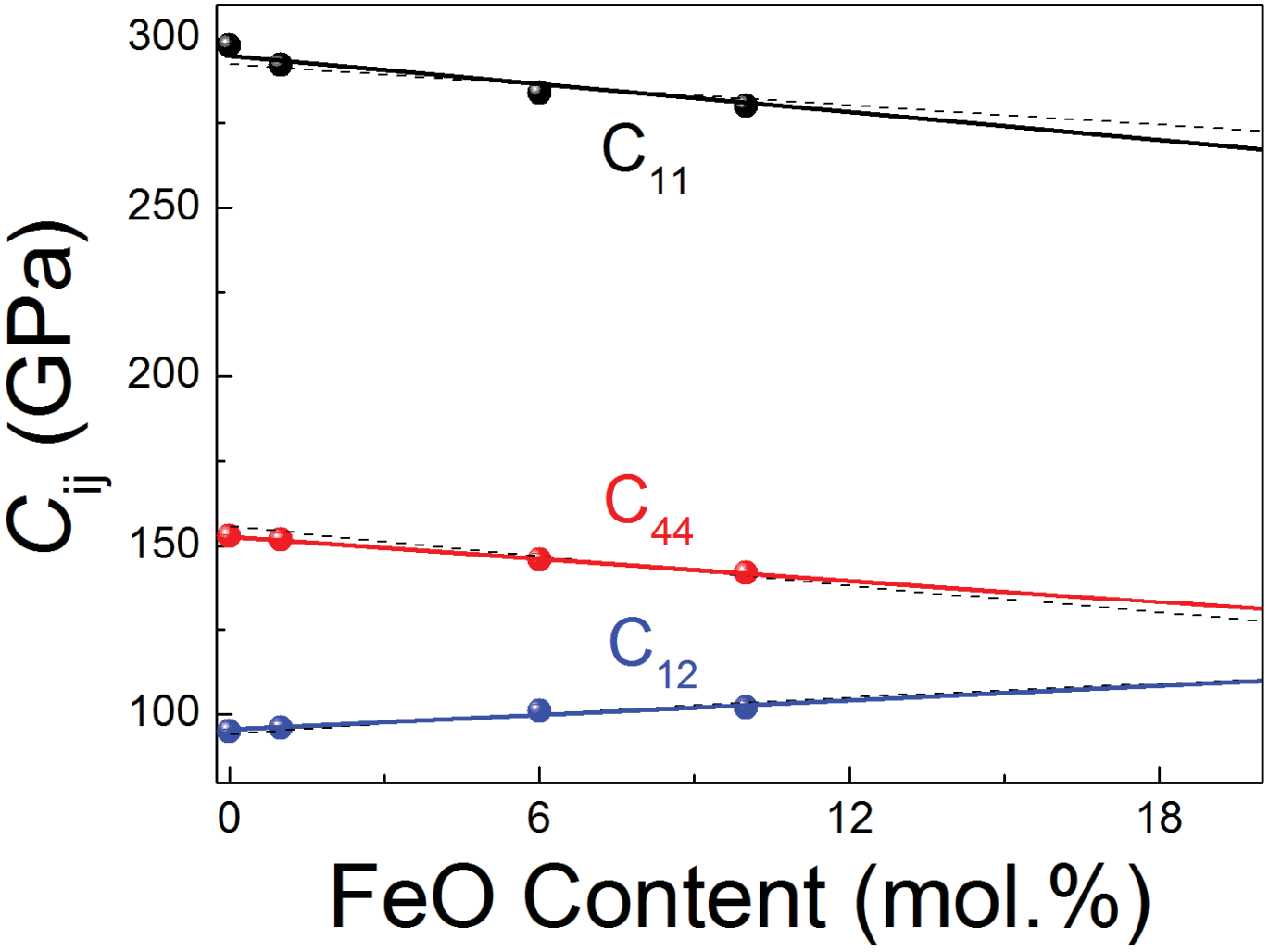

Ā

Ä !"Ā*Ā

This is a preprint, the final version is subject to change, of the American Mineralogist (MSA)
Cite as Authors (Year) Title. American Mineralogist, in press.
DOI: https://doi.org/10.2138/am-2019-6656

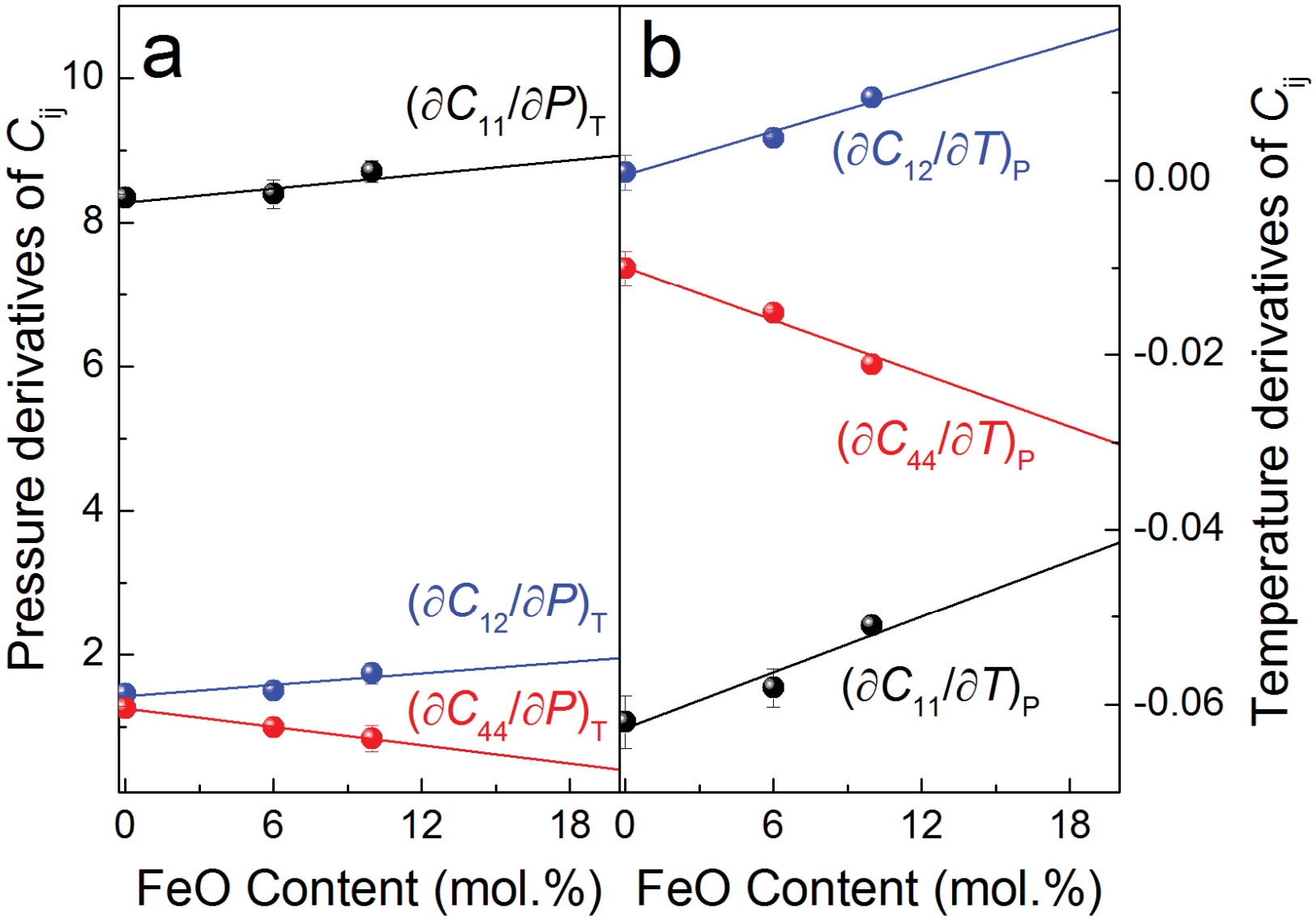

This is a preprint, the final version is subject to change, of the American Mineralogist (MSA)
Cite as Authors (Year) Title. American Mineralogist, in press.
DOI: https://doi.org/10.2138/am-2019-6656

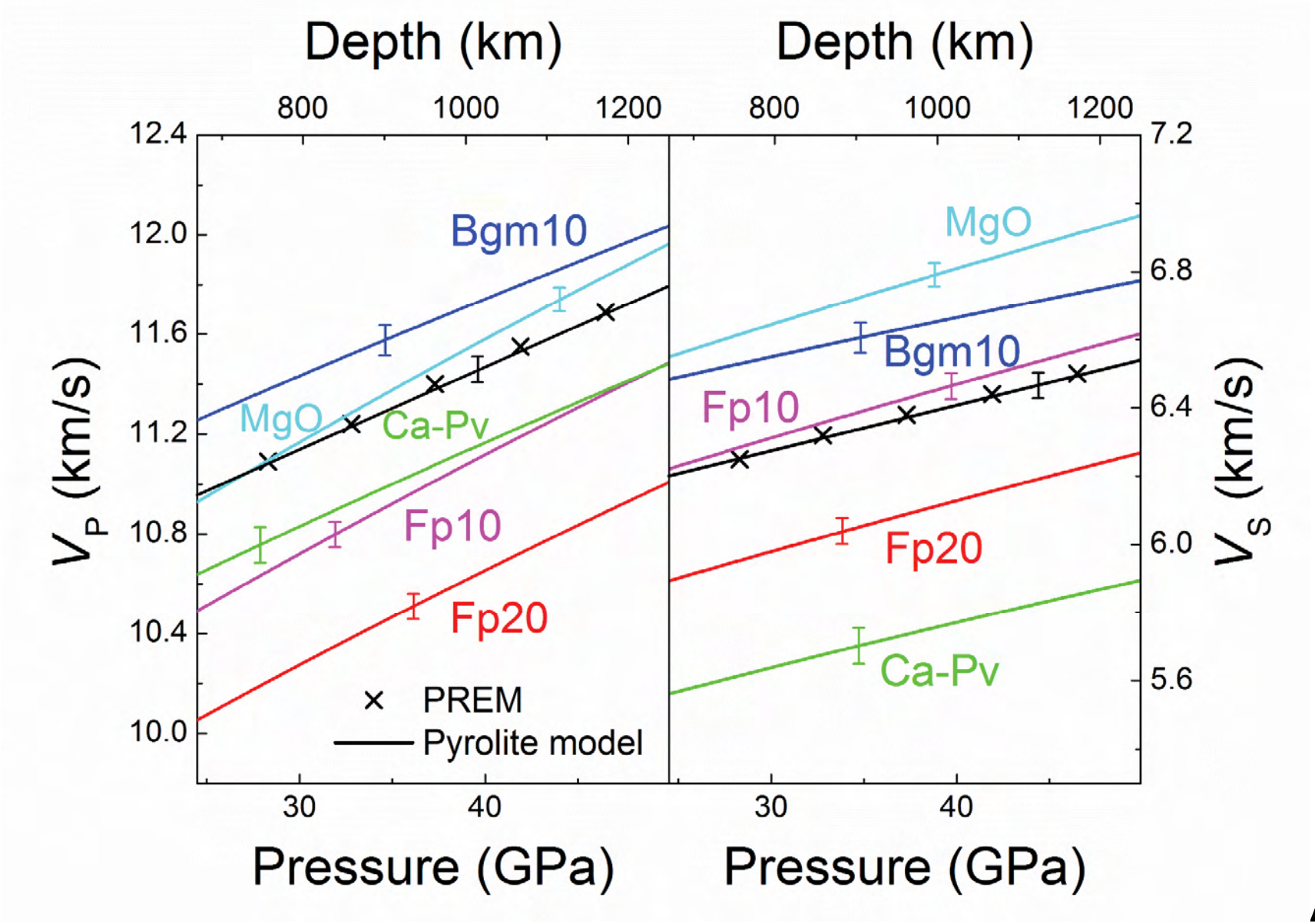

Ā

À !"Ā#,Ā

This is a preprint, the final version is subject to change, of the American Mineralogist (MSA)
Cite as Authors (Year) Title. American Mineralogist, in press.
DOI: https://doi.org/10.2138/am-2019-6656

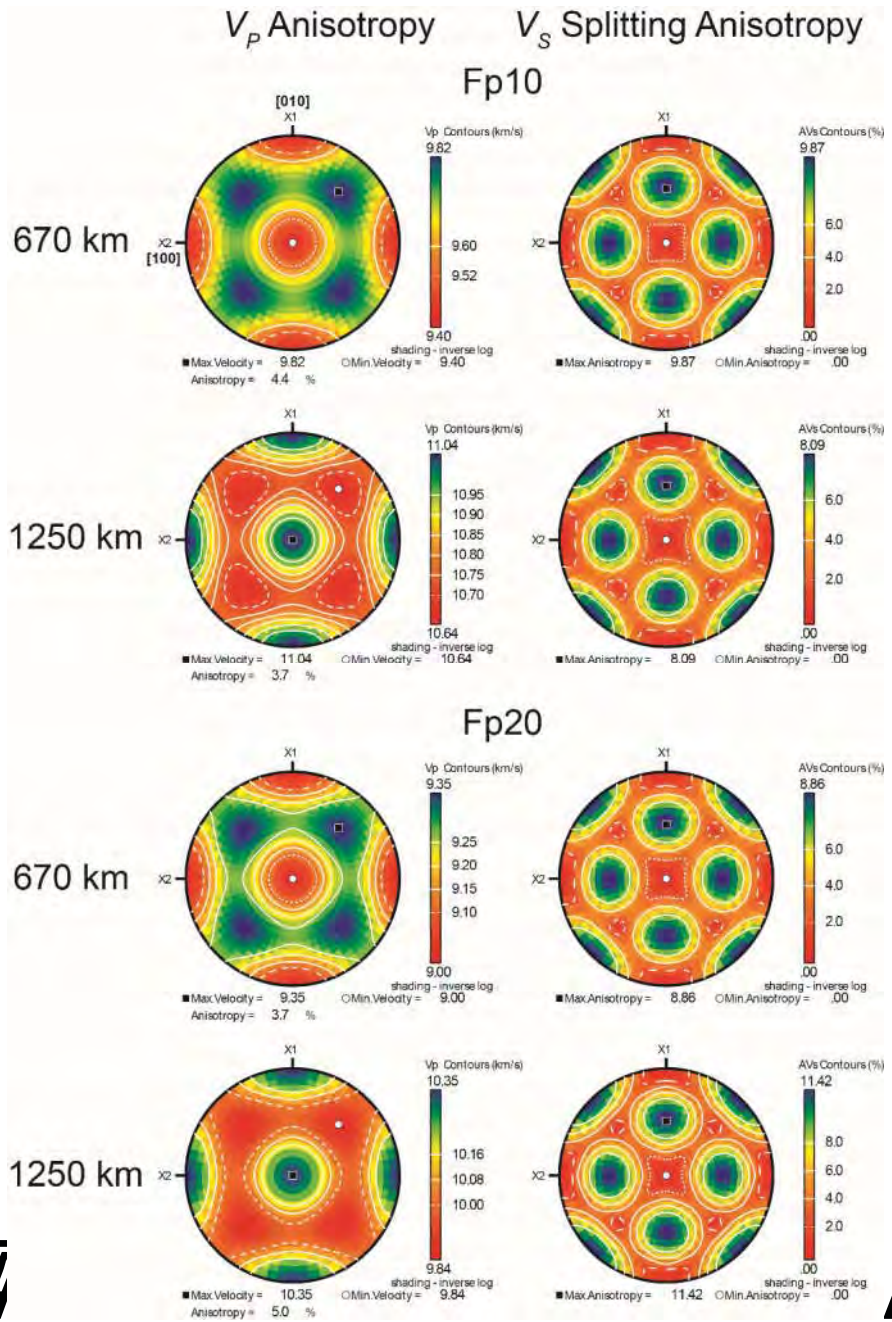

This is a preprint, the final version is subject to change, of the American Mineralogist (MSA)
Cite as Authors (Year) Title. American Mineralogist, in press.
DOI: https://doi.org/10.2138/am-2019-6656

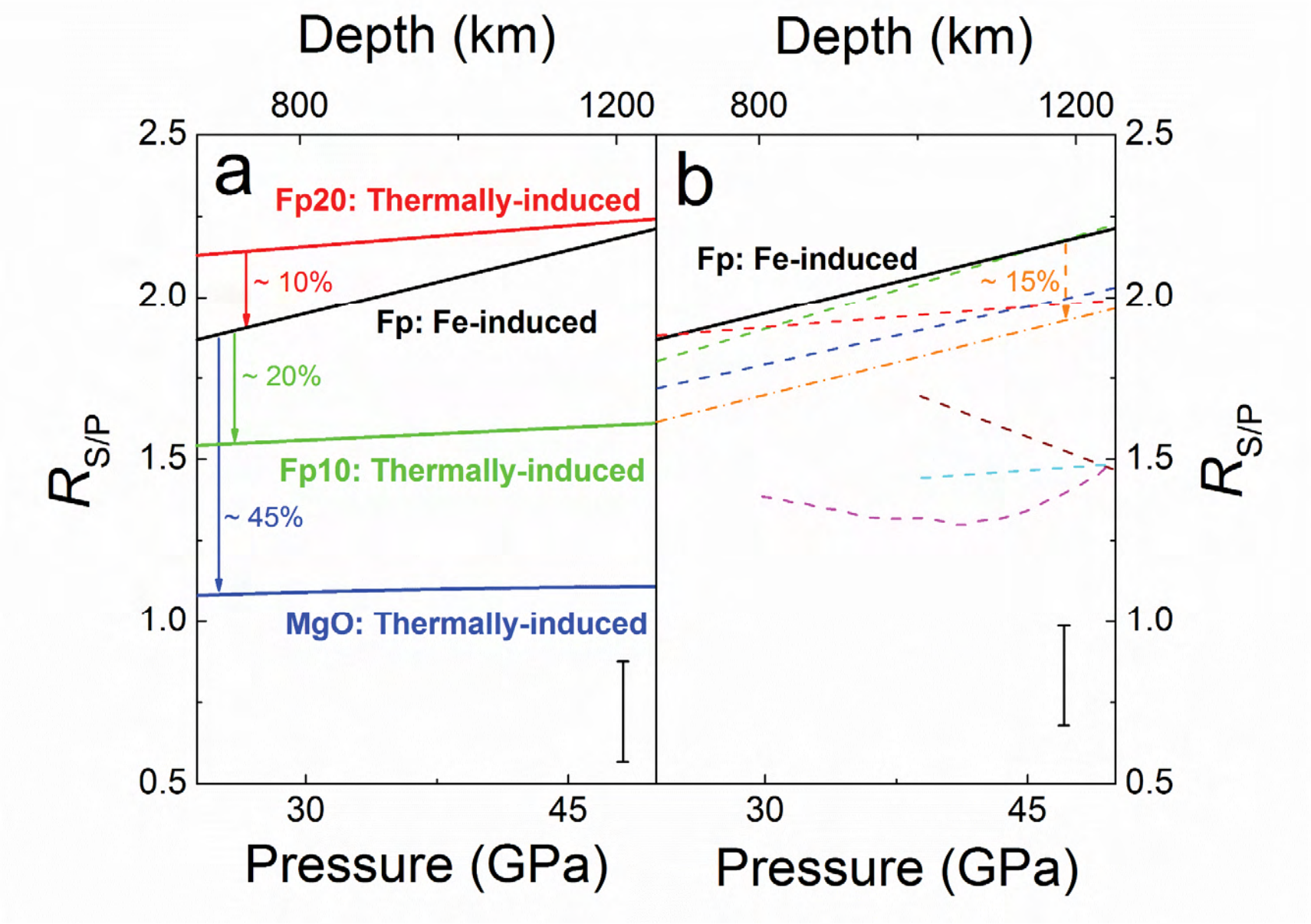

Ā

À !"Ā#$Ā